

Size effect and lateral pressure effect on the mechanical resistance of columnar jointed basalt

Yong-yi Wang^a, Bin Gong^{b,*}, Chun-an Tang^a, Xiao-yu Yang^c

^a State Key Laboratory of Coastal and Offshore Engineering, Dalian University of Technology, Dalian, 116024, PR China

^b College of Engineering, Design and Physical Sciences, Brunel University London, London, UB8 3PH, United Kingdom

^c School of Civil Engineering, Chongqing Jiaotong University, Chongqing, 400074, PR China

ARTICLE INFO

Keywords:

Columnar jointed basalts
Size effect
Lateral pressure effect
Failure mode
Numerical investigation

ABSTRACT

To reveal the size effect and lateral pressure effect of columnar jointed basalts (CJBs), the meso-damage mechanics, statistical strength theory, continuum mechanics and digital image correlation are combined, and a series of heterogeneous numerical models of CJBs orthogonal and parallel to column axis are established. The elastic modulus, Poisson's ratio, uniaxial compressive strength, friction angle, residual strength coefficient, heterogeneity index of basalts 60 GPa, 0.2, 120 MPa, 56.15°, 0.1 and 5, respectively. The gradual fracture processes and acoustic emission characteristics of CJBs suffering various lateral pressures are numerically simulated under the axial loading rate of 0.05 mm/min, and the influence of model size on the anisotropy and lateral pressure effect of CJBs is analyzed. The results show that: for the direction I/II orthogonal to column axis, when the lateral pressure is 2 MPa and 6 MPa, the critical value of size effect is 4 m and 6 m, respectively; for the direction parallel to column axis, the compressive strength of specimen can be obviously improved by increasing lateral pressure for the certain sizes; when the lateral pressure is 6 MPa and the distance ratio of the secondary joint set is 0% or 50%, the compression strengths of the 3 m and 6 m specimens change in a U-shape and a V-shape with the column dip angle increasing, respectively. The results can contribute to understanding the non-linear deformation and failure behaviors of CJBs.

1. Introduction

Columnar joints are a kind of typical tensile fracture structures widely existing in basalts. It often cuts basalts into regular hexagonal prisms or other irregular prisms. Meanwhile, CJB (columnar jointed basalt) or CJRM (columnar jointed rock mass) are popularly distributed in the world, such as in China, Mexico, Australia, Brazil, India, Scotland, Siberia, the United States, etc.^{1–4} In the past decades, the CJBs (or CJRMs) have been encountered at some hydropower plants in southwest China.^{5–7} The observed field photographs^{8,9} of CJBs are shown in Fig. 1.

Some researchers^{10–13} analyzed the anisotropy, size effect and lateral pressure effect of bedded rocks. For the field test of CJBs, valuable results have been obtained; but the environment of engineered rock masses in field test is often complex. Meanwhile, sampling rock specimen would be influenced by disturbance. The field measurement, scanning electron microscope (SEM), back-analysis method as well as numerical simulation were applied by Hao et al.¹⁴ to investigate the time-dependent evolution of the excavation-induced damaged zone

around underground openings in CJRMs. An in situ microseismic monitoring experiment was carried out by Xiao et al.¹⁵ to understand the fracturing process in CJRMs as a result of tunnel excavation. The geometrical structures and fracture patterns of the CJRMs at a dam foundation was reported by Jiang et al.,¹ and a systematic field test for the CJRMs was also carried out on the dam foundation using ultrasonic *P* wave measurements. Three types of joints with different macro- and micro-characteristics from the CJRMs were identified by Jiang et al.¹⁶ using scanning electron microscopy. The attenuation characteristics of the microseismic signals in the CJRM tunnel were studied by Chen et al.,¹⁷ as well as the types and characteristics of the CJRM fracture. The rock cracking indices for improved tunnel support design were suggested by Feng et al.,¹⁸ and the approach has been applied to calculate the thickness of shotcretes, the time consuming of installing rock-bolts, and so on, for the large diversion excavations in CJRMs at the hydro-power station in China.

In terms of the laboratory tests, valuable results reflecting the mechanical responses of jointed rock masses have been obtained; but it is

* Corresponding author.

E-mail address: bin.gong@brunel.ac.uk (B. Gong).

<https://doi.org/10.1016/j.ijmms.2023.105571>

Received 15 December 2021; Received in revised form 18 July 2023; Accepted 4 September 2023

Available online 15 September 2023

1365-1609/© 2023 The Authors. Published by Elsevier Ltd. This is an open access article under the CC BY license (<http://creativecommons.org/licenses/by/4.0/>).

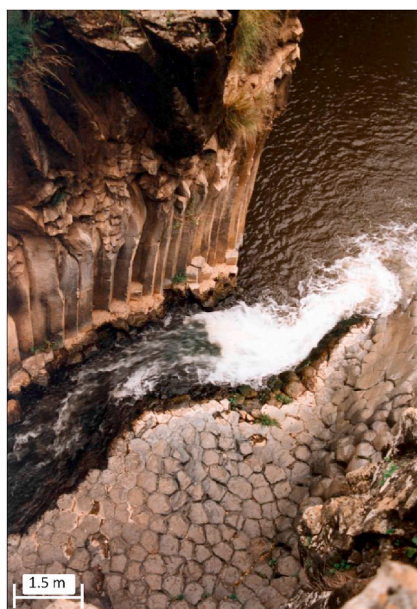
difficult to consider the mechanical parameters of the actual joint surface in the laboratory physical test. When many specimens and scenarios are necessary, the large cost of time and money is unavoidable. Lin et al.³ carried out a group of uniaxial compression tests to investigate the anisotropic characteristic and fracture modes of irregular CJRMs. A series of physical tests were performed by Jin et al.¹⁹ to understand the anisotropic CJRM properties. The strength behavior and deformation modulus of CJRM were investigated by Lin et al.,²⁰ in which the artificial physical model samples with different column dip angles and heights of specimen were considered. Uniaxial tests were performed by Que et al.⁴ on the artificial CJRM samples containing columnar structures to model the mechanical behavior of the CJRMs. To model the mechanical behavior of the CJRM, the artificial CJRM specimens with geological structure similar with that found in the actual CJRMs were compressed under uniaxial load by Ji et al.²¹ To reveal the hydro-mechanical behavior of the Baihetan CJRMs, triaxial compression experiments were conducted by Xiang et al.⁷ on the samples containing regular hexagonal columns.

In terms of the numerical simulations, the insightful achievements^{22–24} have been achieved regarding the size effect and anisotropy of jointed rock masses; however, there are few systematic studies on the effects of different rock homogeneities, column diameters, joint mechanical properties, rock meso constitutive laws and model boundaries on the size effect and lateral pressure effect of CJBs. For the CJBs at the Baihetan dam, the quadrangular, pentagonal and hexagonal prism constitutive models were adopted by Niu et al.²⁵ to compute the permeability index of CJRMs suffering varying deflection angles, and then the permeability anisotropy features of the three models were discussed through numerical simulations. Using the bisection method, a modified Lloyd's algorithm was developed by Meng et al.²⁶ to create the Voronoi diagram. Simulation of the CJRMs by six parameters was therefore proposed, and the related case study of CJRMs was performed to prove the effectiveness of this method. A homogenization-based modeling method was developed by Meng et al.⁶ to investigate the influences of columnar jointed structure on the mechanical behaviors of rocks. The parametric study illustrated that the elastic indices of CJRMs were greatly affected by the columnar joints. Yan et al.²⁷ applied the fast Lagrangian analysis of continua (FLAC) to model the mechanical resistance of CJRMs involving varying column angles. The strength and

elastic indices were gained to analyze the deformation and resistance of rock mass subject to the conventional and true triaxial compression. Discrete element analysis was conducted by Zou et al.⁵ to estimate the size of hydraulic representative volume element of CJRMs.

However, the majority of the above studies didn't systematically consider the effect of model boundaries, the variation of joint mechanical properties and rock meso constitutive relations on the size effect and the lateral effect of CJB, or the progressive fracture processes were not reproduced appropriately. CJB shows obvious discontinuity, heterogeneity, anisotropy and size effect. As a special structural rock mass, the mechanical behavior of CJB/CJRM shows typical nonlinearity, anisotropy, discontinuity and heterogeneity because of the formation of columnar joints. Because of the discontinuity and heterogeneity, their strength is generally lower than intact rock. The anisotropy of CJBs is also affected by size effect. In the practical projects, rock masses generally suffer lateral pressure. Thus, it is also of great practical significance to summarize the deformation and strength of CJBs under lateral pressure, and the related treatments of engineered rock mass.

In this study, to understand the fracture mechanisms of CJBs affected by the size effect and lateral pressure effect, the combination of the digital image correlation (DIC), meso-damage mechanics, statistical strength theory, and continuum mechanics was employed. By transforming the digital images of CJB specimens into inhomogeneous models, a series of numerical tests were conducted, and the validity and reliability of the simulations were verified by comparing the simulated results with the relevant experimental data. Furthermore, the progressive fracture processes and failure patterns of CJBs, both orthogonal and parallel to the column axis, were successfully reproduced under varying lateral pressures. Additionally, the influence of various factors, such as the elastic modulus of joints, the distance ratio of the secondary joint set, the rock meso constitutive relation, the irregular degree of columns and the model boundaries, on the mechanical response of CJBs were comprehensively discussed to shed light on the intricate relationship between these parameters and the fracture mechanisms of CJBs.



(a)



(b)

Fig. 1. The field photographs of CJBs (or CJRMs): (a) the CJRMs in Israel⁸; (b) the CJRMs in Santa Maria Regla, Hidalgo State, Mexico.⁹

2. Numerical modeling

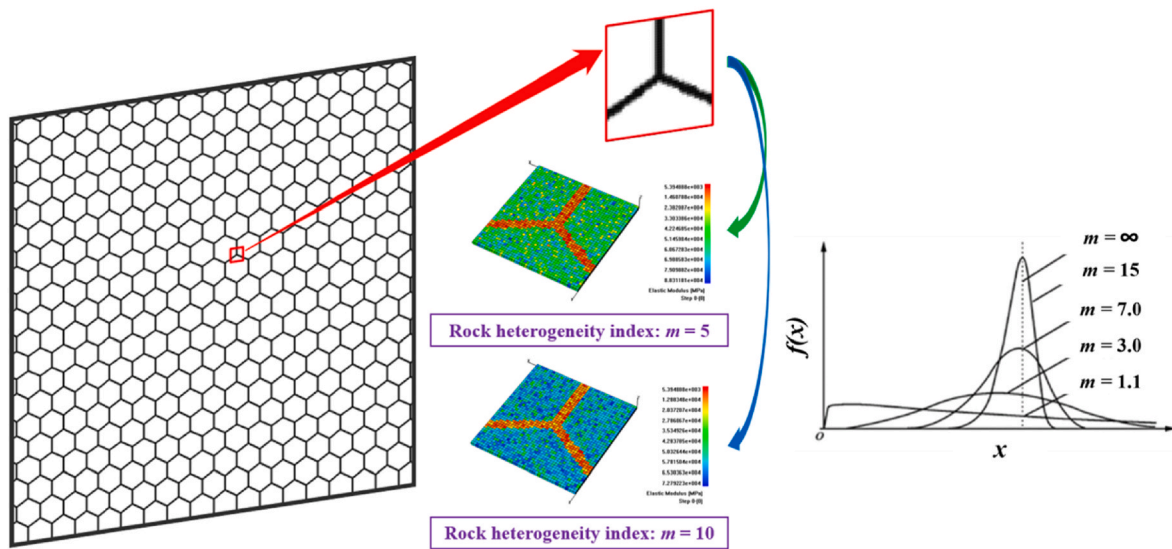
2.1. Rationale of the DIC-improved RFPA method

The main advances of the rock failure process analysis (RFPA) method lie in modeling the progressive failure process without assuming when and where the new cracks will generate and how they will propagate and connect with each other.²⁸⁻³¹ In addition, the validity and reliability of the RFPA code have been assessed in a number of typical laboratory tests on idealized jointed rock samples to evaluate the anisotropic behavior of jointed rock samples.³²⁻³⁴ RFPA also has been widely applied in investigating the slope stability,^{35,36} scale effect³⁷ and anisotropy^{38,39} of jointed rock masses at field scales. Therefore, RFPA is an effective tool to investigate the anisotropic behavior of jointed rock masses.

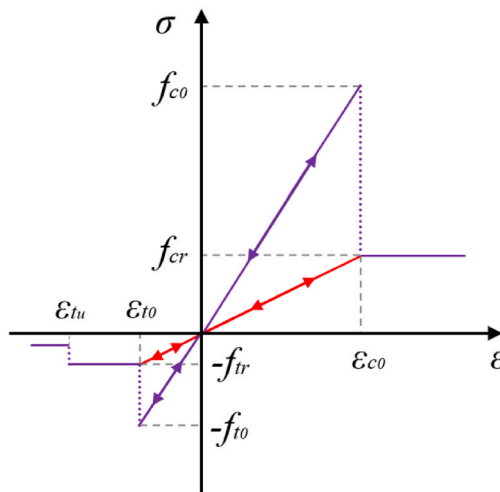
The digital image correlation (DIC) is combined with the RFPA method to improve the model building capability. Clearly, the image

import, gray threshold segmentation and pixel processing are added into the RFPA method. In order to build a numerical model, it is necessary to transform the information of the digital images into the vectorized data for modeling. The digital image is composed of square pixels. In 3D space, if the image is considered to have a certain thickness, each pixel can be regarded as a finite element mesh. The corner coordinates of each pixel are transformed into the physical positions of the corresponding element. According to the gray value of each pixel, it is classified into joint or rock material and assigned corresponding material parameters. According to the above principle, the schematic diagram of transforming digital image into heterogenous numerical model is presented in Fig. 2 (a).

The elastic-brittle damage constitutive law of element under uniaxial stress is depicted in Fig. 2 (b). According to the method of extending one-dimensional constitutive relation under uniaxial stress to complex stress conditions, which was proposed by Mazars and Pijaudier-Cabot⁴⁰ for a constitutive relation of elastic damage, we can easily extend the



(a)



(b)

Fig. 2. (a) The schematic diagram of transforming digital image into heterogenous numerical model; (b) the elastic-brittle damage constitutive relation of element under uniaxial stress.

constitutive relation described above to a three-dimensional stress state.

2.2. Failure criteria and damage behavior of meso element

In the DIC-improved RFPA code, the heterogeneity of material properties is considered when the mechanical parameters of numerous finite elements are assumed to follow the Weibull distribution:

$$f(u) = \frac{m}{u_0} \left(\frac{u}{u_0}\right)^{m-1} \exp\left(-\frac{u}{u_0}\right)^m \quad (1)$$

where u represents the various mechanical parameters of individual elements such as Poisson's ratio, compressive strength or elastic modulus, u_0 is the corresponding mean value of the elements for the specimen and m , known as the heterogeneity index, determines the shape of $f(u)$ and represents the degree of heterogeneity. Generally, a higher m represents a lower heterogeneity.

When an element is under uniaxial tension, the elastic-brittle damage constitutive relation will be adopted. The tensile damage function can be described using the following inequality:

$$\sigma_3 \leq f_t \quad (2)$$

where f_t is the uniaxial tensile strength. In this paper, the compressive stresses and strains are taken as positive.

Simultaneously, the Mohr-Coulomb criterion is applied to determine whether a meso element is damaged in the shear mode, and it can be expressed as follows:

$$\sigma_1 - \frac{1 + \sin \varphi}{1 - \sin \varphi} \sigma_3 - f_c \geq 0 \quad (3)$$

where σ_1 and σ_3 are the major and minor principal stresses of the meso element, respectively, and φ and f_c are the internal friction angle and uniaxial compressive strength.

In RFPA, the mechanical responses of rocks and joints are modelled by finite elements. The dilation can be calculated by the accumulated local deformation of the elements satisfying the failure criteria. When the compression happens at the joints and the compression strain of the joint elements reaches the ultimate compressive strain threshold, the elastic moduli of the joint elements will be improved exponentially to avoid penetration.^{28–31}

In elastic damage mechanics, when the value of the stress increases to a specific value leading to the failure of the element, the elastic modulus of an element will degrade gradually as the damage evolves. The elastic modulus of the damaged material can be defined as follows:

$$E = (1 - D)E_0 \quad (4)$$

where D represents the damage variable, E represents the elastic modulus of the damaged material element, and E_0 represents the elastic modulus of the undamaged material element.

Tensile damage will occur when the maximum tensile strain criterion is satisfied. According to the constitutive law, the damage variable D can be expressed as follows.⁴¹

$$D = \begin{cases} 0 & \varepsilon > \varepsilon_{t0} \\ 1 - \frac{\lambda \varepsilon_{t0}}{\varepsilon} & \varepsilon_{tu} < \varepsilon \leq \varepsilon_{t0} \\ 1 & \varepsilon \leq \varepsilon_{tu} \end{cases} \quad (5)$$

where λ is the coefficient of residual strength given by $\lambda = f_{tr}/f_t$, f_t is the uniaxial tensile strength, f_{tr} is the residual tensile strength, ε_{t0} is the elastic limit strain (or tensile threshold strain) given by $\varepsilon_{t0} = f_t/E_0$, and ε_{tu} is the ultimate tensile strain describing the state when an element is fully damaged. The ultimate tensile strain can be defined as $\varepsilon_{tu} = \eta \varepsilon_{t0}$, where η is termed the ultimate strain coefficient.

Additionally, when a meso element is damaged in shear, the variable

D can be calculated as follows:⁴¹

$$D = \begin{cases} 0 & \varepsilon < \varepsilon_{c0} \\ 1 - \frac{\lambda \varepsilon_{c0}}{\varepsilon} & \varepsilon \geq \varepsilon_{c0} \end{cases} \quad (6)$$

where λ is also the coefficient of residual strength given by $\lambda = f_{cr}/f_c$, f_c is the uniaxial compressive strength, f_{cr} is the residual compressive strength, and ε_{c0} is the compressive threshold strain and given by $\varepsilon_{c0} = f_c/E_0$. In addition, in the DIC-improved RFPA code, the acoustic emission (AE) count and related energy are proportional to the number of damaged elements.

2.3. Validation of the numerical modeling

The laboratory physical experiment of Ke et al.² is adopted to verify the numerical method. Ke et al.² used a mixture of cement, fine sand, water and water reducer as the model materials to make columns. The mass ratio of cement: fine sand: water: water reducer = 1.0: 0.5: 0.35: 0.002. A regular hexagonal prism with a section diameter of 10 mm and a length of 50 mm was selected to simulate the actual column. The white cement slurry with water-cement ratio of 0.4:1.0 was used to bond columns, which simulates joint surface. The ratio of longitudinal to transverse of column was 5. The shift distance of transverse joint was 25 mm. Seven kinds of column dip angles were considered ($\beta = 0^\circ, 15^\circ, 30^\circ, 45^\circ, 60^\circ, 75^\circ, 90^\circ$). The rock mass specimens were regular quadrangular prism specimens with the size of 50 mm × 50 mm × 100 mm. The uniaxial compression tests were carried out by using the CSS-3940YJ rock mechanics servo testing machine. The loading method with constant displacement rate was adopted in the experiment, and the loading rate was 0.05 mm/min. A flat steel cushion block was placed at the upper and lower ends of the specimen, and then axial pressure was applied at a constant displacement rate until failure of the specimen occurred.

In this paper, the specimens used for numerical verification were rectangular specimens with a width of 50 mm and a height of 100 mm as plane strain case. The diameter of the hexagonal prism inside the specimen was 10 mm. The directions I and II orthogonal column axis and the directions parallel to column axis ($\beta = 0^\circ-90^\circ$ with interval of 15°) were considered. The digital images were converted into finite element mesh models, as shown in Table 1. The mechanical parameter values of the finite element models were presented in Table 2, which was referred to the relevant literatures^{15,18,20,25,27} of CJBs. The displacement-controlled loading was used in the numerical test, in which the loading amount was 0.005mm/step until the failure of specimen appeared.

The comparison of normalized uniaxial compression strength coefficients between laboratory physical test and numerical test is depicted in Fig. 3. In addition, the comparison of the specimen failure patterns between the laboratory physical test and the numerical test is presented in Table 3. It can be seen that the results of laboratory physical tests and numerical tests show relatively good similarity.

2.4. Numerical configuration

In this study, the finite element numerical specimens were sourced from the CJBs at the Baihetan Hydropower Station in China. The column length is 0.5~3 m, and the diameter is 13~25 cm. As shown in Table 4, the specimens in numerical test are square models but own different sizes of 0.5 m, 1 m, 2 m, 3 m, 4 m, 6 m, and 8 m, respectively. The elastic modulus of joints is 3.75 GPa, 7.5 GPa, 15 GPa, 22.5 GPa, 30 GPa, respectively, as depicted in Fig. 4 (a). The residual strength coefficients of rock are taken as 0.1, 0.5, 0.75 and 1, respectively, which reflects the gradual transformation of the mechanical constitutive law of rock from brittleness to plasticity, as presented in Fig. 4 (b). The dip angles of the column are $0^\circ, 15^\circ, 30^\circ, 45^\circ, 60^\circ, 75^\circ$ and 90° , respectively. The spacing

Table 1

The schematic diagram of joint setting, geometric parameters and loading conditions of the digital images and corresponding finite element models in numerical simulation verification.

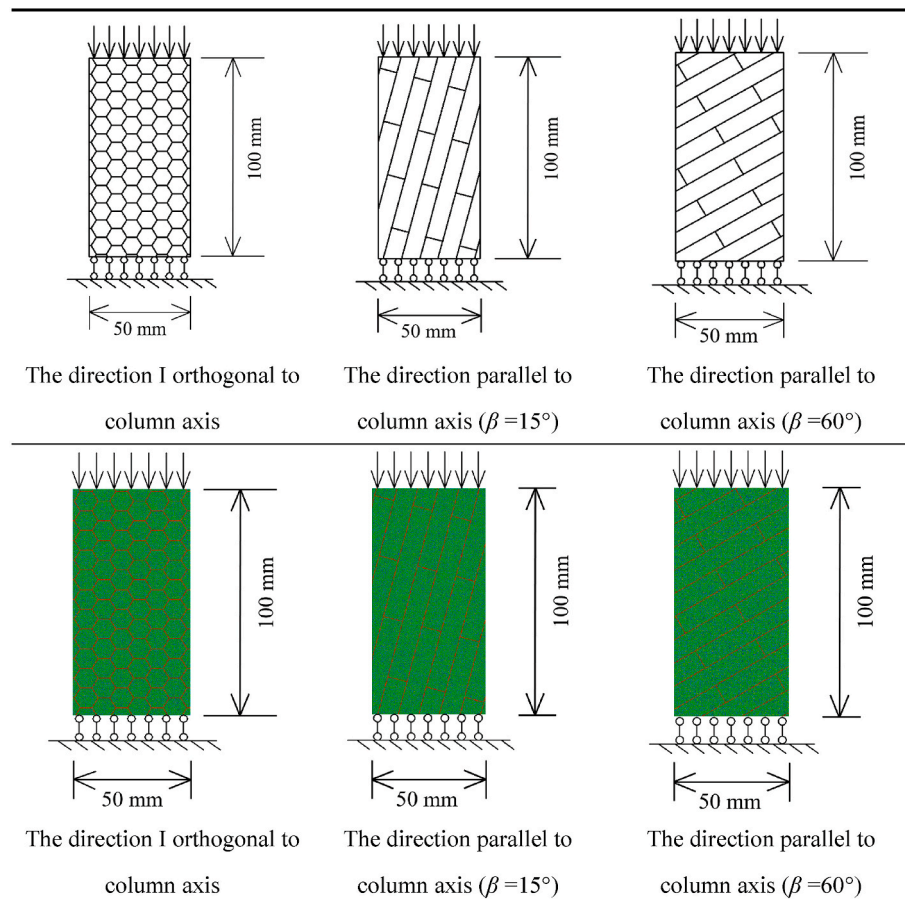


Table 2

The mechanical parameter values of finite element model in validation of numerical simulation.

Material type	Heterogeneity index	Elastic modulus (GPa)	Poisson's ratio	Uniaxial compressive strength (MPa)	Friction angle (°)	Residual strength coefficient
Basalt	5	60	0.2	120	56.15	0.1
Joint	5	15	0.25	30	36	1

of the secondary joint set is 1.5 m, and the distance ratios of the secondary joint set are 0% and 50%. As shown in Fig. 4 (d), the distance ratio of the secondary joint set is defined to be L/S_2 . The irregularity degrees of columns are considered as completely regular columns, approximately regular columns, moderately regular columns, and irregular columns, respectively. For the boundary conditions of model, two kinds of model boundaries are considered when calculating the size effect and lateral pressure effect of CJBs: the case of plane strain, the case between plane stress and plane strain.

Through a series of numerical trials, it can be found that when the average length of element edges reaches 5 mm and the mesh is relatively regular and symmetrical, the effect of mesh on the deformation and failure of the CJB models can be ignored. Meanwhile, to further eliminate the effect of mesh, the element size of each model basically keeps the same in the following simulations. Taking 6 m specimen as an example, the number of elements of the specimen is 2,433,600. Fig. 5 (a)&(b) show the diagrams of the CJBs along the directions I and II orthogonal to column axis. The typical setup and boundary condition for numerical test of CJBs specimens along the direction parallel to column axis are presented in Fig. 5 (c)~(g). For Fig. 5 (f), the hinge support

constraints are set on two faces along two normal directions of the model, which means that normal displacements along two normal directions are constrained; for Fig. 5 (g), the hinge support constraint is set on one face along a normal direction of the model, which means that one normal displacement along the normal direction is constrained, another normal displacement along the other normal direction is free. For Fig. 5 (c)~(g), a load was applied to the top of each model along the vertical direction with the displacement-controlled mode. The ratio of the displacement applied per step to the initial lateral side length of model is 0.000017. The displacement load is applied gradually until the model failures.

Generally, the mechanical parameters of joint are lower than intact rock.⁴² The selection of joint parameter values would influence the magnitude of the elastic modulus and compression strength of rock mass.⁴³ However, the ratios of mechanical properties between joint and intact rock have not been reported yet. Based on the above numerical verification and related literatures^{15,18,20,25,27} of CJBs, the mechanical parameter values of joint are determined, and the mechanical parameter values of rock and joint of CJBs are listed in Table 5.

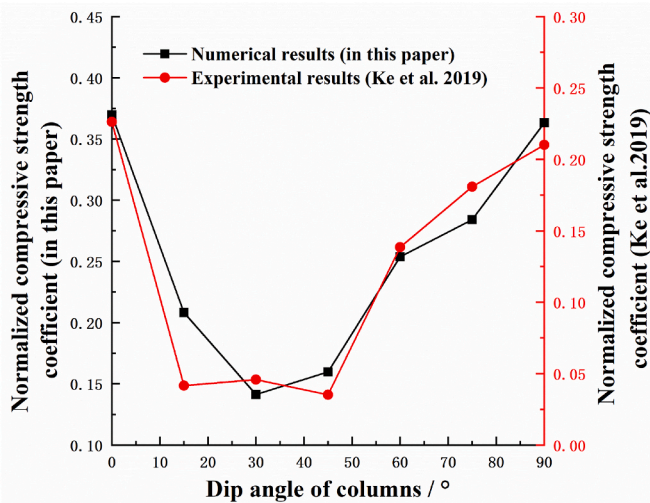


Fig. 3. The comparison of normalized uniaxial compression strength coefficients between laboratory physical tests and numerical tests.

3. Results and analysis

3.1. Influence of model size on anisotropy and lateral pressure effect of CJBs

3.1.1. Influence of model size on anisotropy and lateral pressure effect of CJBs orthogonal to column axis

As shown in Fig. 6 (a), in terms of compressive strength (CS), for the case of direction I orthogonal to column axis, when the lateral pressure is 0 MPa, the CS of specimen changes gently with the increase of model size; when the lateral pressure is 2 MPa and 6 MPa, the CS of specimen firstly decreases and then changes gently with the growth of model size. The critical value of size effect is 4 m when the lateral pressure is 2 MPa, and 6 m when the lateral pressure is 6 MPa. For the case of direction II orthogonal to column axis, when the lateral pressure is 0 MPa, the CS of specimen changes gently with the increase of model size. When the lateral pressure is 2 MPa, the CS of specimen decreases in a stair way with the growth of model size, and the critical value of size effect is 4 m; when the lateral pressure is 6 MPa, the CS of specimen firstly decreases and then changes gently with the increase of model size, and the critical value of size effect is 6 m.

As depicted in Fig. 6 (b), in the aspect of equivalent deformation modulus (EDM), for the case of direction I orthogonal to column axis, when the lateral pressure is 0 MPa, the EDM of specimen firstly increases, then fluctuates, and then gradually increases with the increase of model size; when the lateral pressure is 2 MPa, the EDM grows firstly and then decreases gradually; when the lateral pressure is 6 MPa, the EDM of specimen fluctuates. For the case of direction II orthogonal to column axis, when the lateral pressure is 0 MPa, the EDM firstly fluctuates and then increases with the growth of model size; when the lateral pressure is 2 MPa and 6 MPa, the EDM of specimen fluctuates.

3.1.2. Influence of model size on anisotropy and lateral pressure effect of CJBs parallel to column axis

As presented in Fig. 6 (c), in terms of CS, for the case of the lateral pressures of 0 MPa, 2 MPa and 6 MPa and the specimen size of 4 m, the CS of specimen is obviously improved with the increase of lateral pressure at the column dip angles of 0°–90°. When the lateral pressure is 6 MPa and the specimen size is 0.5 m, 1 m, 2 m, 3 m and 4 m, the CS of specimen decreases roughly with the increase of specimen size at the column dip angles of 0°–90°. The corresponding polar diagram for the CS of CJBs is depicted in Fig. 6 (e).

As shown in Fig. 6 (d), in the aspect of EDM, for the case of the lateral

pressures of 0 MPa, 2 MPa, 6 MPa and the specimen size of 4 m, the EDM of specimen firstly decreases and then grows with the growth of lateral pressure at the column dip angles of 0°–90°, and reaches the minimum value at the column dip angle of 60°. When the lateral pressure is 6 MPa and the specimen size is 0.5 m, the EDM of specimen firstly decreases and then fluctuates with the increase of column dip angle, and reaches the minimum at the column dip angle of 30°; when the specimen size is 1 m, the EDM of specimen changes in rough V-shape way with the growth of column dip angle, and reaches the minimum value when column dip angle is 30°; when the specimen size is 2 m, 3 m and 4 m, the EDM of specimen firstly decreases and then grows with the increase of column dip angle, and reaches the minimum value at column dip angle of 60°. The corresponding polar diagram for the EDM of CJBs is displayed in Fig. 6 (f).

Fig. 7 (a)–(g) show the z-direction displacement diagrams of the CJBs with model sizes of 0.5 m × 0.5 m, 1 m × 1 m, 2 m × 2 m, 3 m × 3 m, 4 m × 4 m, 6 m × 6 m and 8 m × 8 m, respectively, along the direction I orthogonal to column axis, under the lateral pressure of 2 MPa. According to Fig. 7 (a)–(g), for the CJBs with model size of 0.5 m × 0.5 m, the cracks initiate and propagate at the column sections, and the sedimentation inside the specimen is distributed along the cracks. When the size of the specimen is 1 m × 1 m, the columns are broken at the upper part of the specimen, and the sedimentation is distributed along the fracture zone. For the CJBs with model size of 2 m × 2 m, there are fractured columns at the upper and lower parts of the specimen. At the upper part of the specimen, the sedimentation is mainly distributed along the fracture zone with sharp angle characteristic. When the size of the specimen is 3 m × 3 m, the column fractures are developed at the upper and lower parts of the specimen. The sedimentation inside the specimen is mainly distributed along the fluctuating fracture zone at the upper part of the specimen. For the CJBs with model size of 4 m × 4 m, the vertical joints get cracked and the columns are broken at the upper part of the specimen. There are weak trends of vertical joint cracking at the left and right sides of the lower part of the specimen. The sedimentation is distributed along the fracture zone with sharp angle characteristic at the upper part of the specimen. When the size of the specimen is 6 m × 6 m, the vertical joint cracking mainly occurs at the upper part of the specimen, and the column fractures are obvious at the middle of the upper part of the specimen. The sedimentation inside the specimen is characterized by shallow sedimentation transfer at the middle of the upper part of the specimen and deep sedimentation transfer at the left and right sides of the upper part of the specimen. For the CJBs with model size of 8 m × 8 m, at the middle of the upper part of the specimen, the vertical joints get cracked, and the column fractures are also obvious at the middle of the upper part of the specimen. The sedimentation transfer at the middle of the upper part of the specimen is shallow, and that at the left and right sides of the upper part of the specimen is relatively deep.

Fig. 7 (h)–(n) display the z-direction displacement diagrams of the CJBs with model size of 4 m × 4 m, column dip angles of $\beta = 0^\circ, 15^\circ, 30^\circ, 45^\circ, 60^\circ, 75^\circ$ and 90° , respectively, along the direction parallel to column axis, under the lateral pressure of 2 MPa. According to Fig. 7 (h)–(n), for the CJBs with $\beta = 0^\circ$, the columnar joints are cracked and the columns get broken at the upper part of the specimen. The sedimentation inside the specimen is mainly distributed along the fracture zone. When the column dip angle is $\beta = 15^\circ$, the columnar joints at the upper part of the specimen get slipped and cracked, and the sedimentation distribution inside the specimen is relatively uniform. For the CJBs with $\beta = 30^\circ$, the columnar joints are slipped and cracked. At the top of the specimen, and the middle and upper part of the specimen, the cracks initiate and develop at the edges of several columns, forming strip fracture zones. The sedimentation at the right side of the upper part of the specimen is relatively obvious. When the column dip angle is $\beta = 45^\circ$, there is still an obvious strip fracture zone inside the specimen, and the sedimentation at the right side of the upper part of the specimen is

Table 3
The comparison of failure patterns between numerical tests and laboratory physical tests.

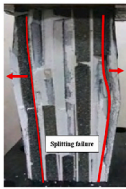
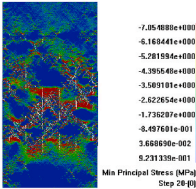
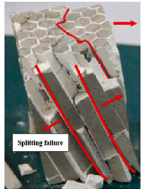
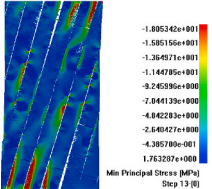

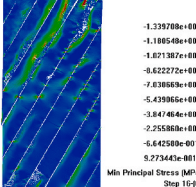

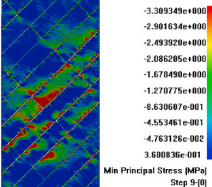
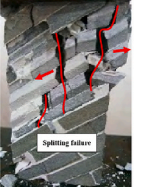
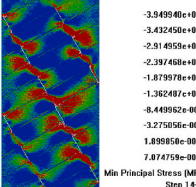

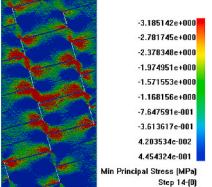
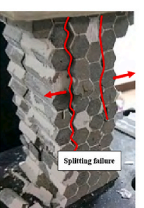
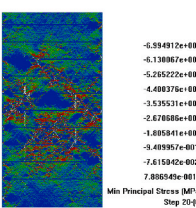
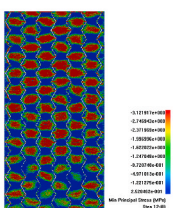
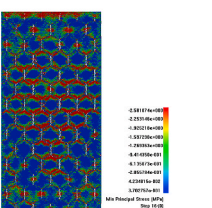
			
<p>The failure pattern of the specimen with $\beta = 0^\circ$, in laboratory physical tests (Ke et al.²)</p>	<p>The minimum principal stress diagram of the specimen with $\beta = 0^\circ$, in numerical tests (in this paper)</p>	<p>The failure pattern of the specimen with $\beta = 15^\circ$, in laboratory physical tests (Ke et al.²)</p>	<p>The minimum principal stress diagram of the specimen with $\beta = 15^\circ$, in numerical tests (in this paper)</p>
			
<p>The failure pattern of the specimen with $\beta = 30^\circ$, in laboratory physical tests (Ke et al.²)</p>	<p>The minimum principal stress diagram of the specimen with $\beta = 30^\circ$, in numerical tests (in this paper)</p>	<p>The failure pattern of the specimen with $\beta = 45^\circ$, in laboratory physical tests (Ke et al.²)</p>	<p>The minimum principal stress diagram of the specimen with $\beta = 45^\circ$, in numerical tests (in this paper)</p>
			
<p>The failure pattern of the specimen with $\beta = 60^\circ$, in laboratory physical tests (Ke et al.²)</p>	<p>The minimum principal stress diagram of the specimen with $\beta = 60^\circ$, in numerical tests (in this paper)</p>	<p>The failure pattern of the specimen with $\beta = 75^\circ$, in laboratory physical tests (Ke et al.²)</p>	<p>The minimum principal stress diagram of the specimen with $\beta = 75^\circ$, in numerical tests (in this paper)</p>
			
<p>The failure pattern of the specimen with $\beta = 90^\circ$, in laboratory physical tests (Ke et al.²)</p>	<p>The minimum principal stress diagram of the specimen with $\beta = 90^\circ$, in numerical tests (in this paper)</p>	<p>The minimum principal stress diagram of the specimen along the direction I orthogonal to column axis, in numerical tests (in this paper)</p>	<p>The minimum principal stress diagram of the specimen along the direction II orthogonal to column axis, in numerical tests (in this paper)</p>

Table 4

The parameter values and calculation condition settings of numerical test on size effect and lateral pressure effect of CJBs.

	Parameter values and calculation condition settings
Lateral pressure (MPa)	0, 2, 4, 6, 8
Model size along the direction orthogonal to column axis (m)	0.5 × 0.5, 1 × 1, 2 × 2, 3 × 3, 4 × 4, 6 × 6, 8 × 8
Column dip angle β along the direction parallel to column axis ($^{\circ}$)	0, 15, 30, 45, 60, 75, 90
Elastic modulus of joints (GPa)	3.75, 7.5, 15, 22.5, 30
Residual strength coefficient of joints	1
The distance ratio of the secondary joint set (%)	0, 50
Residual strength coefficient of rock	0.1, 0.5, 0.75, 1
The irregularity degree of columns	Completely regular columns, approximately regular columns, moderately regular columns and irregular columns.
Model boundaries	The case of plane strain, the case between plane stress and plane strain.

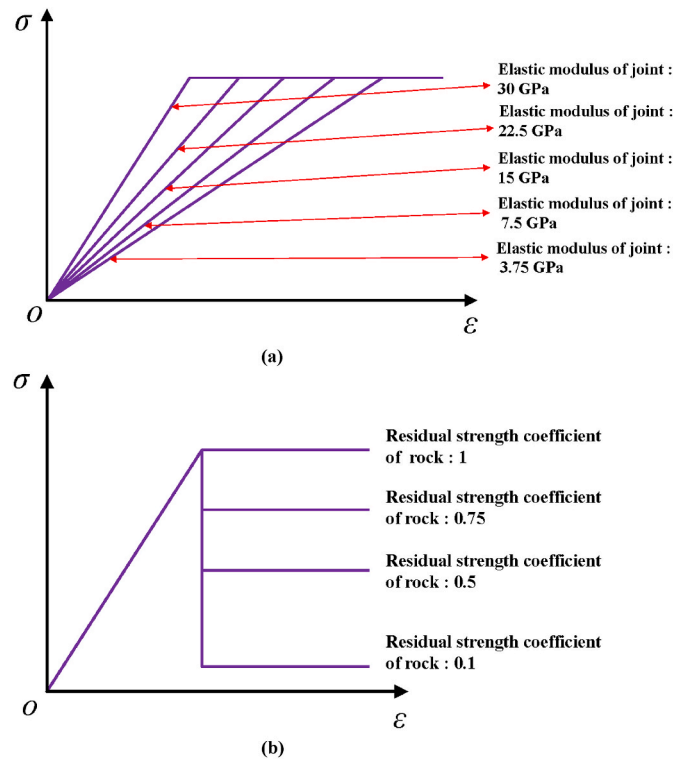


Fig. 4. (a) The constitutive relation of joint with different elastic moduli; (b) the constitutive relation of rock with different residual strength coefficients.

still relatively obvious. For the CJBs with $\beta = 60^{\circ}$, at the middle and upper part of the specimen, cracks initiate and develop at the edges of several columns, and oblique strip fracture zones are formed near the top of the specimen, and the sedimentation is distributed along the fracture zones. When the column dip angle is $\beta = 75^{\circ}$, at the upper part of the specimen, the oblique fracture zones initiate and develop, and the sedimentation is mainly distributed along the fracture zones. For the CJBs with $\beta = 90^{\circ}$, the crushing is developed at the upper part of the specimen, and the sedimentation inside the specimen is characterized by shallow sedimentation transfer at the middle of the upper part of the specimen and relatively deep sedimentation transfer at the left and right sides of the upper part of the specimen.

3.2. Progressive failure process and failure pattern of CJBs with lateral pressure

3.2.1. Progressive failure process and failure pattern of CJBs with lateral pressure along the direction I orthogonal to column axis

3.2.1.1. Lateral pressure of 0 MPa. Fig. 8 (a) displays the schematic diagram of the CJBs model in the case of plane strain, along the direction I orthogonal to column axis under lateral pressure of 0 MPa. Fig. 8 (b)~(g) show the stress-strain curve of 6 m specimen, and the minimum principal stress diagrams at Points A, B, C, D, E, F, G, H corresponding to the stress-strain curve, which describes the process of crack initiation, propagation and rupture during loading. The red area in the minimum principal stress diagram represents the tensile stress concentration area.

According to Fig. 8 (b)~(g), at Points A and B in the loading stage, as the loading keeps growing, the stress concentration area appears above the triangular region in the specimen, and then the vertical joints at the middle of the upper part of the specimen gradually get cracked, and the stress concentration area gradually narrows. With the loading increasing, the vertical joints at the middle of the upper part of the specimen are cracked obviously, and then the stress concentration mainly appears at the centers of the columns in the middle of the upper part of the specimen. See the minimum principal stress diagram at Point C. When stress reaches to Point D, the original stress concentration area develops to the lower left side and the lower right side. When the stress is loaded to Point E, some columns at the middle of the upper part of the specimen get broken, and the stress concentration area retracts upward, and the stress concentration mainly appears at some columns in the middle of the upper part of the specimen. When the stress is loaded to the peak Point F of the stress-strain curve, more columns at the upper part of the specimen show stress concentration and fracture initiation and propagation. When the stress drops to Point G, the stress concentration develops on the upper left side of the specimen, and then the fracture initiation and propagation occur. When the stress drops to the Point H, the stress concentration appears at the right side of the upper part of the specimen, and then the fracturing initiates and develops. At this time, as a whole, the fracturing at the upper part of the specimen get intensified.

In Fig. 8 (c), in terms of acoustic emission (AE), the AE rate of the specimen shows a double peak distribution. The first AE peak is caused by the damage and cracking of vertical joints; the second AE peak is mainly caused by the fracture of the columns at the upper part of the specimen.

As can be seen from the damage diagram in Fig. 8 (h), at the upper part of the specimen, and the left and right sides of the lower part of the specimen, the vertical joints get damaged and cracked, and at the upper part of the specimen, the columns are damaged and cracked, roughly forming an M-shaped damage and fracture zone. The x-direction displacement diagram in Fig. 8 (i) shows that at the upper part of the specimen, the displacement along the x-direction is relatively symmetrical. As depicted in the z-direction displacement diagram in Fig. 8 (j), the sedimentation transfer at the middle of the upper part of the specimen is shallow, and that at the left and right sides of the upper part of the specimen is relatively deep. The AE diagram in Fig. 8 (k) shows that at the upper part of the specimen, and the left and right sides of the lower part of the specimen, the vertical joints show blue AEs under tensile action. At the middle of the upper part of the specimen, there are both compressive failure AEs and tensile failure AEs (the compression shear is marked in pink AE; the tension is marked in blue AE).

3.2.1.2. Lateral pressure of 6 MPa. Fig. 9 (a) shows the schematic diagram of the CJBs model in the case of plane strain, along the direction I orthogonal to column axis under lateral pressure of 6 MPa. Fig. 9 (b)~(g) display the stress-strain curve of 6 m specimen, and the minimum principal stress diagrams at Points A, B, C, D, E, F, G, H corresponding to

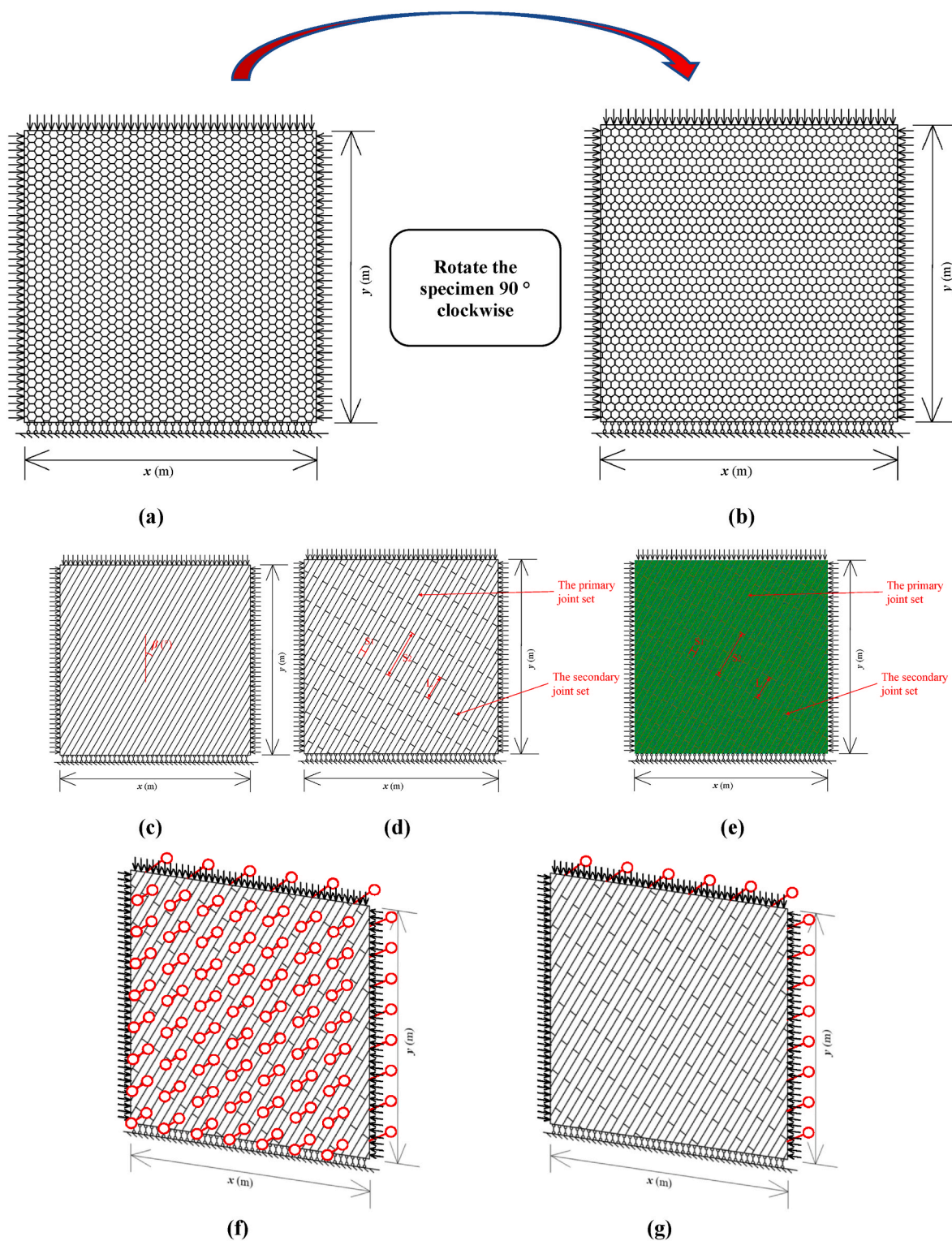
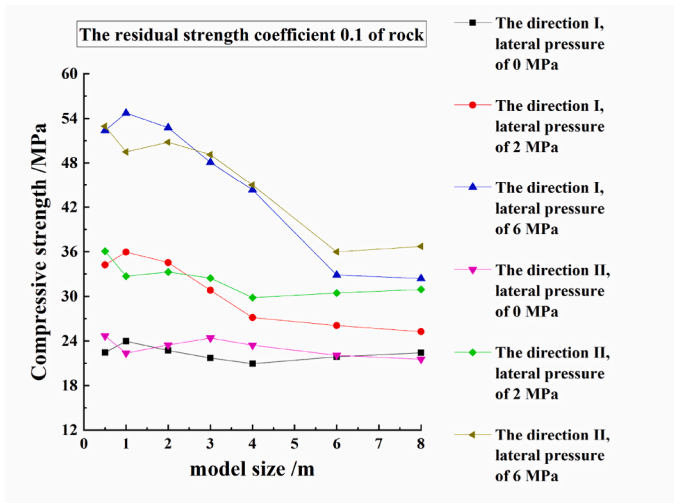


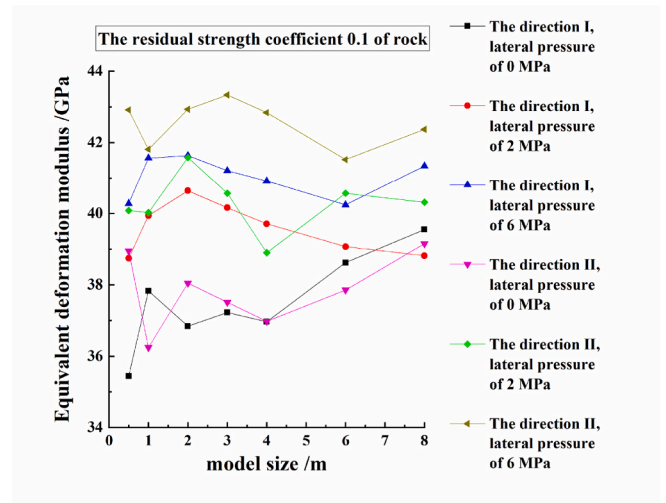
Fig. 5. (a)&(b) The schematic diagram of numerical test of the CJBs along the directions I & II orthogonal to column axis; (c) the typical setup of the CJBs along the direction parallel to column axis; (d)&(e)&(f) the typical setup of the CJBs with transverse joints along the direction parallel to column axis, in the case of plane strain; (g) in the case between plane stress and plane strain.

Table 5
The mechanical parameters of rock and joint in CJBs.

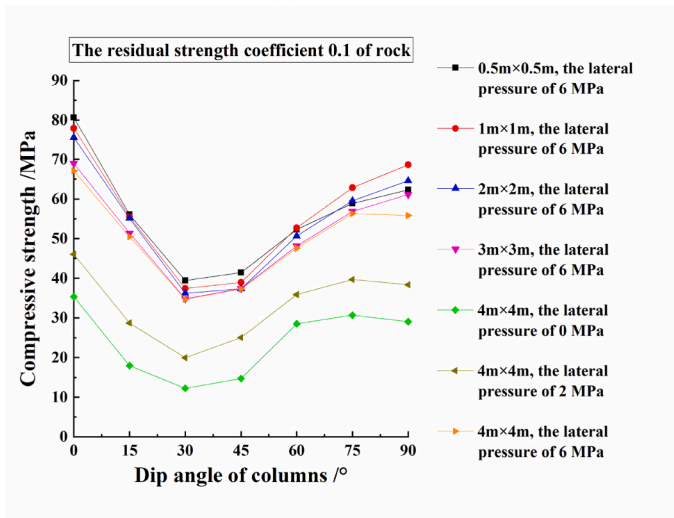
Material type	Heterogeneity index	Elastic modulus (GPa)	Poisson's ratio	Uniaxial compressive strength (MPa)	Friction angle (°)	Residual strength coefficient
Basalt	5	60	0.2	120	56.15	0.1, 0.5, 0.75, 1
Joint	5	3.75, 7.5, 15, 22.5, 30.	0.25	30	36	1



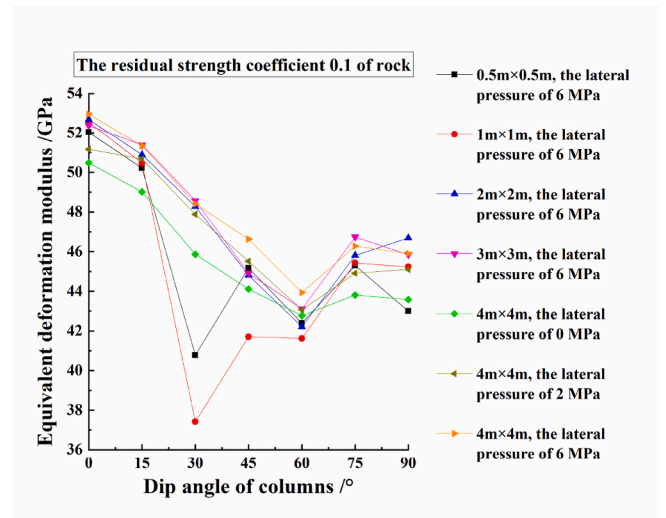
(a)



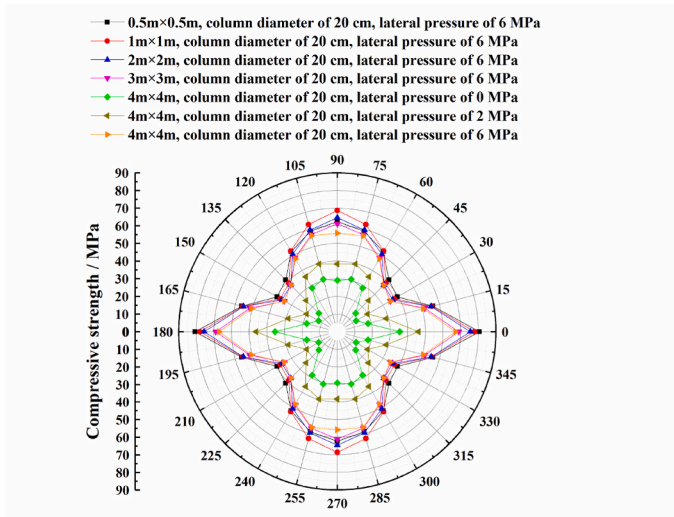
(b)



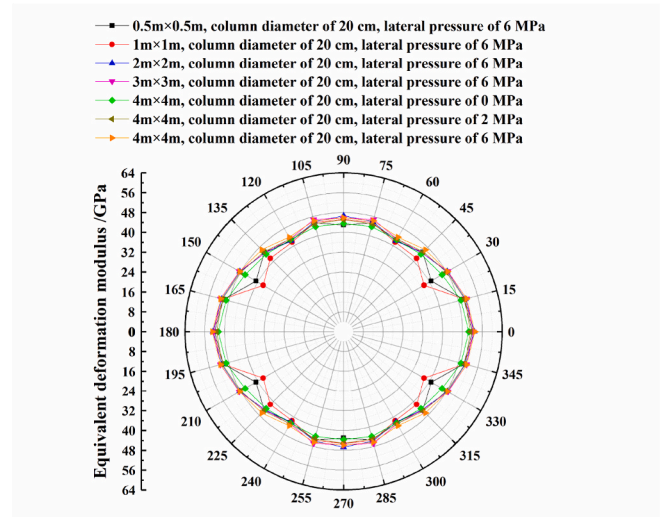
(c)



(d)



(e)



(f)

Fig. 6. (a)&(b) The CSs and EDMs of the specimens with different sizes along the directions I & II orthogonal to column axis; (c)&(d)&(e)&(f) the CSs and EDMs of the specimens with different sizes along the direction parallel to column axis (the rock heterogeneity index 5).

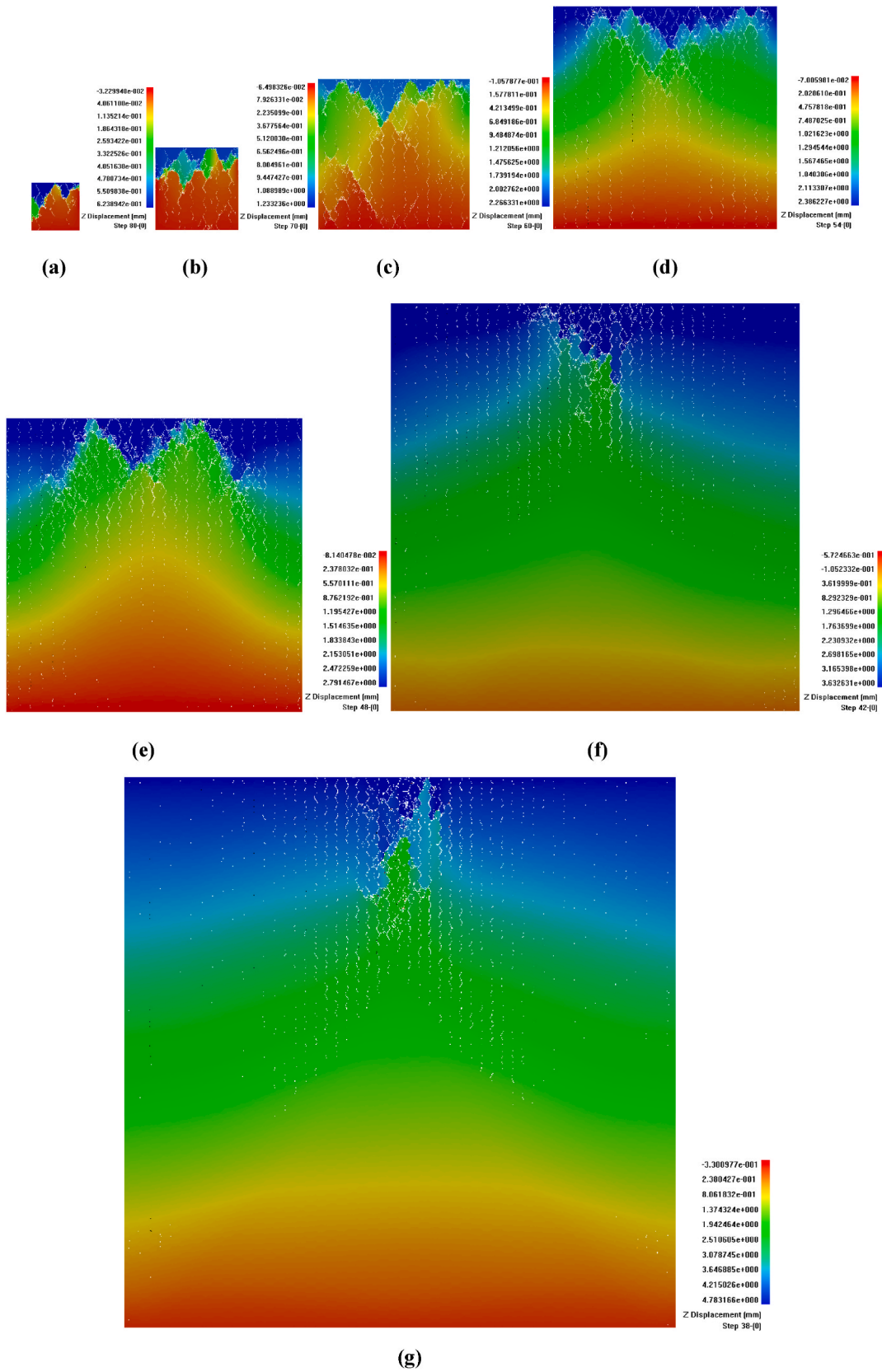


Fig. 7. (a)~(g) Along the direction I orthogonal to column axis, under the lateral pressure of 2 MPa, the z direction displacement diagrams of the CJBs with model sizes of $0.5\text{ m} \times 0.5\text{ m}$, $1\text{ m} \times 1\text{ m}$, $2\text{ m} \times 2\text{ m}$, $3\text{ m} \times 3\text{ m}$, $4\text{ m} \times 4\text{ m}$, $6\text{ m} \times 6\text{ m}$ and $8\text{ m} \times 8\text{ m}$, respectively; (h)~(n) along the direction parallel to column axis, under the lateral pressure of 2 MPa, the z direction displacement diagrams of the CJBs with model size of $4\text{ m} \times 4\text{ m}$, column dip angles of $\beta = 0^\circ$, 15° , 30° , 45° , 60° , 75° and 90° , respectively.

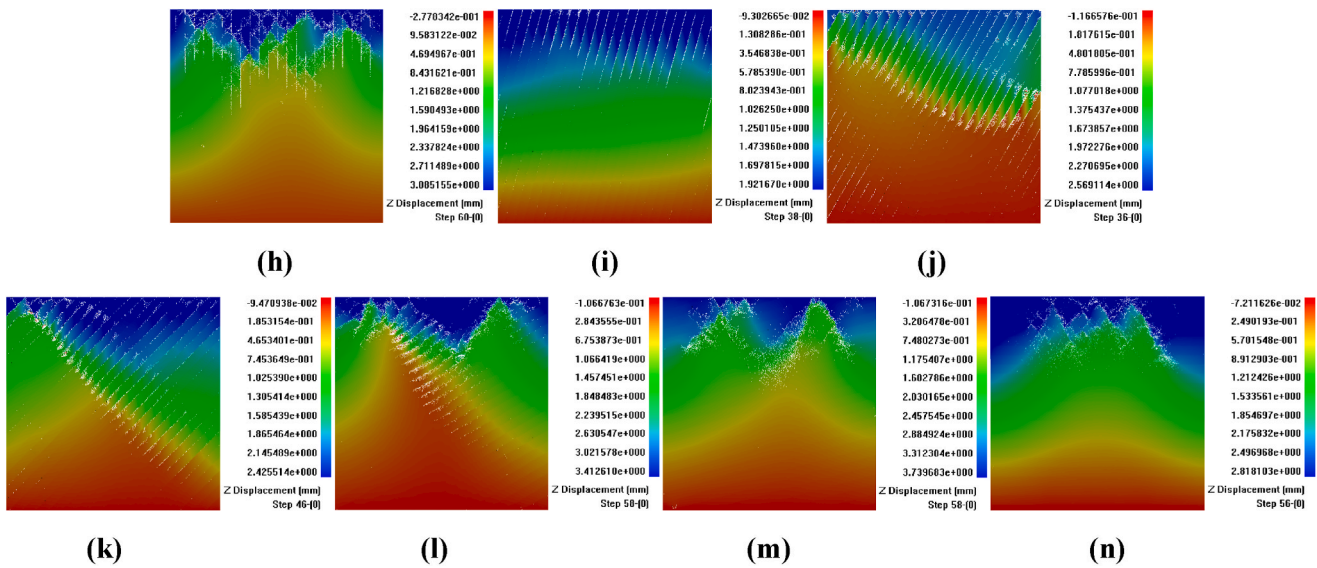


Fig. 7. (continued).

the stress-strain curve. According to Fig. 9 (b)~(g), at Points A and B in the loading stage, with the progress of loading, the stress concentration firstly appears at the vertical joints in the middle of the upper part of the specimen, and then the vertical joints gradually get cracked, and the stress concentrations are transferred to the centers of the nearby columns. When the stress is loaded to Points C and D, the columns at the middle of the upper part of the specimen develops from stress concentration to crack initiation and propagation. When the stress is loaded to Point E, the fracturing of the columns at the middle of the upper part of the specimen is gradually obvious. When the stress is loaded to the peak Point F of the stress-strain curve, the fracturing of the columns at the middle of the upper part of the specimen get intensified. When the stress drops to Point G, the stress concentration appears at the left and right sides of the upper part of the specimen, and then the fracture initiation and propagation occur. When the stress drops to the Point H, the columns at the upper part of the specimen are further broken.

As depicted in Fig. 9 (c), the AE rate of the specimen is also with a double peak distribution. Compared with the lateral pressure of 0 MPa, under the lateral pressure of 6 MPa, the AE peak moves backward on the strain axis, and the distance between the two AE peaks on the strain axis is relatively short. In addition, at the end of loading, the AE rate increases suddenly, indicating the whole specimen in the unstable status.

As presented in the damage diagram in Fig. 9 (h), the damage of the vertical joints is developed at the middle and upper part of the specimen, and the damage and fracture of the columns is obvious at the upper part of the specimen. The x-direction displacement diagram in Fig. 9 (i) shows that at the left and right sides of the upper part of the specimen, the displacement occurs along the opposite direction of the x-direction. As can be seen from the z-direction displacement diagram in Fig. 9 (j), the sedimentation at the middle of the upper part of the specimen is shallow, and that at the left and right sides of the upper part of the specimen is relatively deep. The AE diagram in Fig. 9 (k) shows that at the middle and upper part of the specimen, the vertical joints are subjected to compression shear and tensile action, and pink and blue AEs appear. At the middle of the upper part of the specimen, there are both compressive failure AEs and tensile failure AEs at the columns (the pink AE for compressive shear action and the blue AE for tensile action).

3.2.2. Progressive failure process and failure pattern of CJBs with lateral pressure along the direction II orthogonal to column axis

Fig. 10 (a) shows the schematic diagram of the CJBs model in the case of plane strain, along the direction II orthogonal to column axis under lateral pressure of 6 MPa. Fig. 10 (b)~(g) display the stress-strain

curve of 6 m specimen, and the minimum principal stress diagrams at Points A, B, C, D, E, F, G, H corresponding to the stress-strain curve. Combined with Fig. 10 (b)~(g), it can be seen that at Points A and B in the loading stage, with the progress of loading, the stress concentration appears at the vertical joints in the middle of the upper part of the specimen, and there is a trend of gradual cracking. When the stress is loaded to Point C, the vertical joints at the middle of the upper part of the specimen get cracked, and the stress concentration develops at the nearby oblique joints. When the stress is loaded to Point D, the crack initiation and propagation occur at the columns near the oblique joints at the middle of the upper part of the specimen. When the stress is loaded to the peak Point E of the stress-strain curve, the fracturing of the columns at the middle of the upper part of the specimen is more obvious. When the stress falls to Point F, there are obvious cracking of vertical joints at the upper part of the specimen. When the stress continues to drop to Point G, at the left of upper part of the specimen, the original stress concentration at the columns develops into crack initiation and propagation. When the stress drops to the Point H, the breakage of the columns at the upper part of the specimen is intensified. As shown in Fig. 10 (c), the AE rate of the specimen shows a double peak distribution. Under the lateral pressure of 6 MPa, the distance between the two AE peaks on the strain axis is relatively short. Additionally, at the end of loading, the AE rate increases suddenly, and the whole specimen is unstable.

As can be seen from the damage diagram in Fig. 10 (h), at the upper part of the specimen, the vertical joints are damaged and cracked, the damage of oblique joints is developed, and there are many damaged and broken columns at the upper part of the specimen. The x-direction displacement diagram in Fig. 10 (i) shows that at the left and right sides of the upper part of the specimen, the displacement occurs along the opposite direction of the x-direction. As depicted in the z-direction displacement diagram in Fig. 10 (j), the sedimentation inside the specimen is characterized by shallow sedimentation at the middle of the upper part of the specimen and deep sedimentation at the left and right sides of the upper part of the specimen. The AE diagram in Fig. 10 (k) shows that at the upper part of the specimen, the vertical joints are subjected to tensile action with blue AEs, and the oblique joints are suffered compressive shear action with pink AEs. There are both compressive failure AEs and tensile failure AEs at the upper part of the specimen.

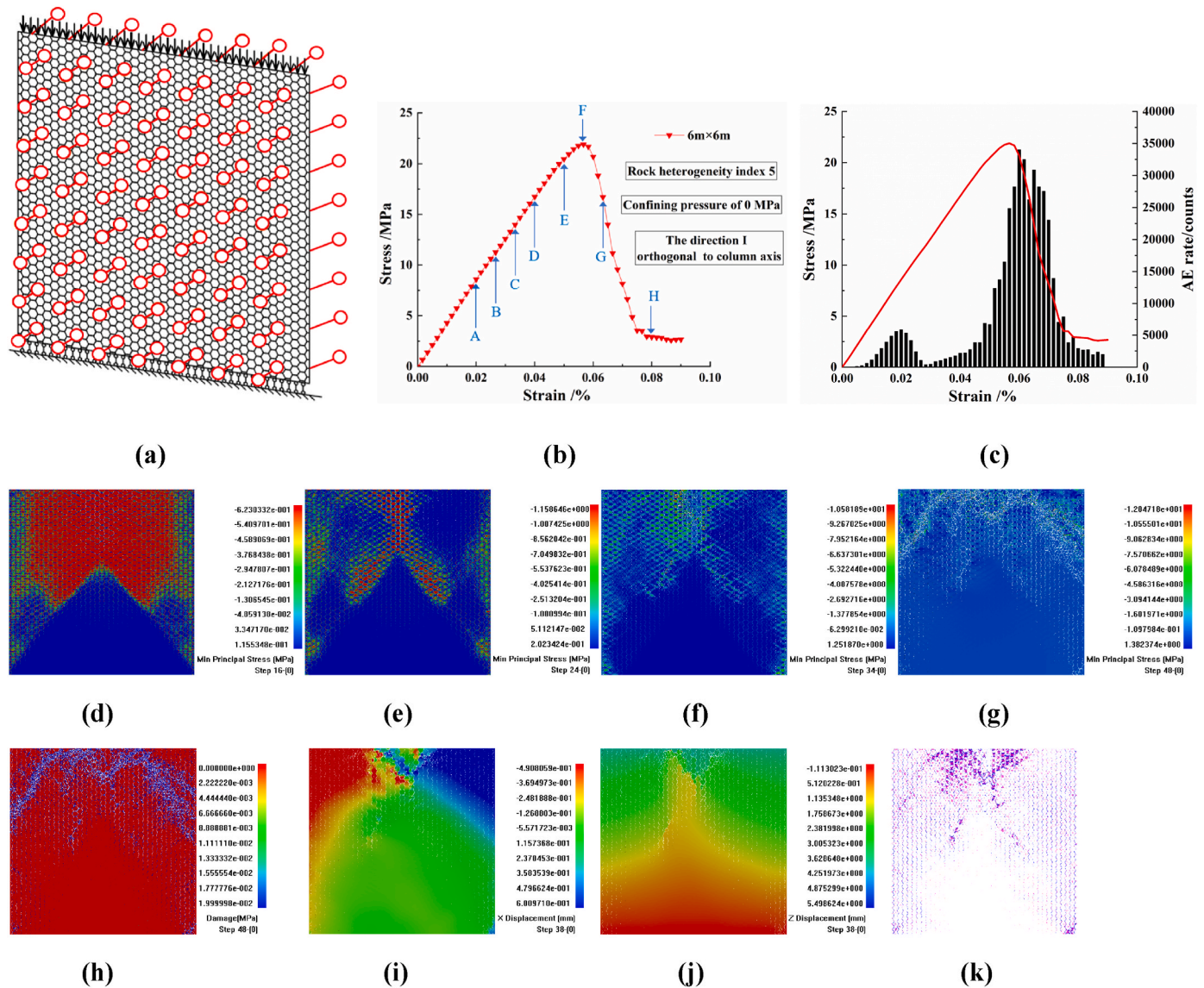


Fig. 8. The progressive failure process and failure pattern along the direction I orthogonal to column axis: (a) the schematic diagram of the CJBs model in the case of plane strain; (b)&(c) the compression stress-strain curve and AE rate; (d)~(g) the minimum principal stress diagrams at Points B, D, F and H corresponding to the stress-strain curve; (h) the damage diagram; (i) the displacement diagram along the x direction; (j) the displacement diagram along the z direction; (k) the AE diagram. (the 6 m specimen with column diameter of 20 cm, heterogeneity index 5, lateral pressure of 0 MPa).

3.2.3. Progressive failure process and failure pattern of CJBs with lateral pressure in the direction parallel to column axis

Fig. 11 (a) shows the schematic diagram of the CJBs model with $\beta = 30^\circ$ in the case of plane strain, along the direction parallel to column axis under lateral pressure of 6 MPa. Fig. 11 (b)~(g) display the minimum principal stress diagrams at Points A, B, C, D, E and F of the stress-strain curve. It can be seen from Fig. 11 (b)~(g) that at Point A of the loading stage, with the progress of loading, the stress concentration appears at columnar joints inside the specimen. When the stress reaches the peak Point B of the stress-strain curve, the trend of compression shear and sliding of columns develops at the top of the specimen. When the stress begins to fall to Point C, the compression shear and sliding of columns further develop, and the stress concentration is obvious at the top of the specimen. When the stress continues to drop to Point D, the stress concentration and crack initiation occur at the edges of several columns in the upper part of the specimen. When the stress drops to Point E, two strip zones with obvious stress concentrations appear inside specimen, in which cracks initiate and propagate at the edges of the columns, and stress concentrations appear at crack tips. When the stress drops to Point

F, the cracks propagate further at the two strip zones with original stress concentration. As presented in Fig. 11 (c), the AE rate of the specimen is roughly in a triple peak distribution. Under the lateral pressure of 6 MPa, at the end of loading, the AE rate increases suddenly, indicating the whole specimen in the unstable status.

As shown in the damage diagram in Fig. 11 (h), the columnar joints inside the specimen are damaged, and near the top of the specimen and at the middle and upper part of the specimen, the damage fracture zones are formed. The x-direction displacement diagram in Fig. 11 (i) shows at the upper part of the specimen and the middle and lower part of the specimen, the displacement occurs along the opposite direction of the x-direction, indicating that the extrusion deformation is serious. As can be seen from the z-direction displacement diagram in Fig. 11 (j), the sedimentation inside the specimen is uneven, and the sedimentation at the right side of the upper part of the specimen is relatively obvious. The AE diagram in Fig. 11 (k) shows that the columnar joints inside the specimen are subjected to compression shear sliding and show pink AEs; near the top of the specimen, there are mainly compressive failure AEs; at the middle and upper part of the specimen, there are mainly tensile failure

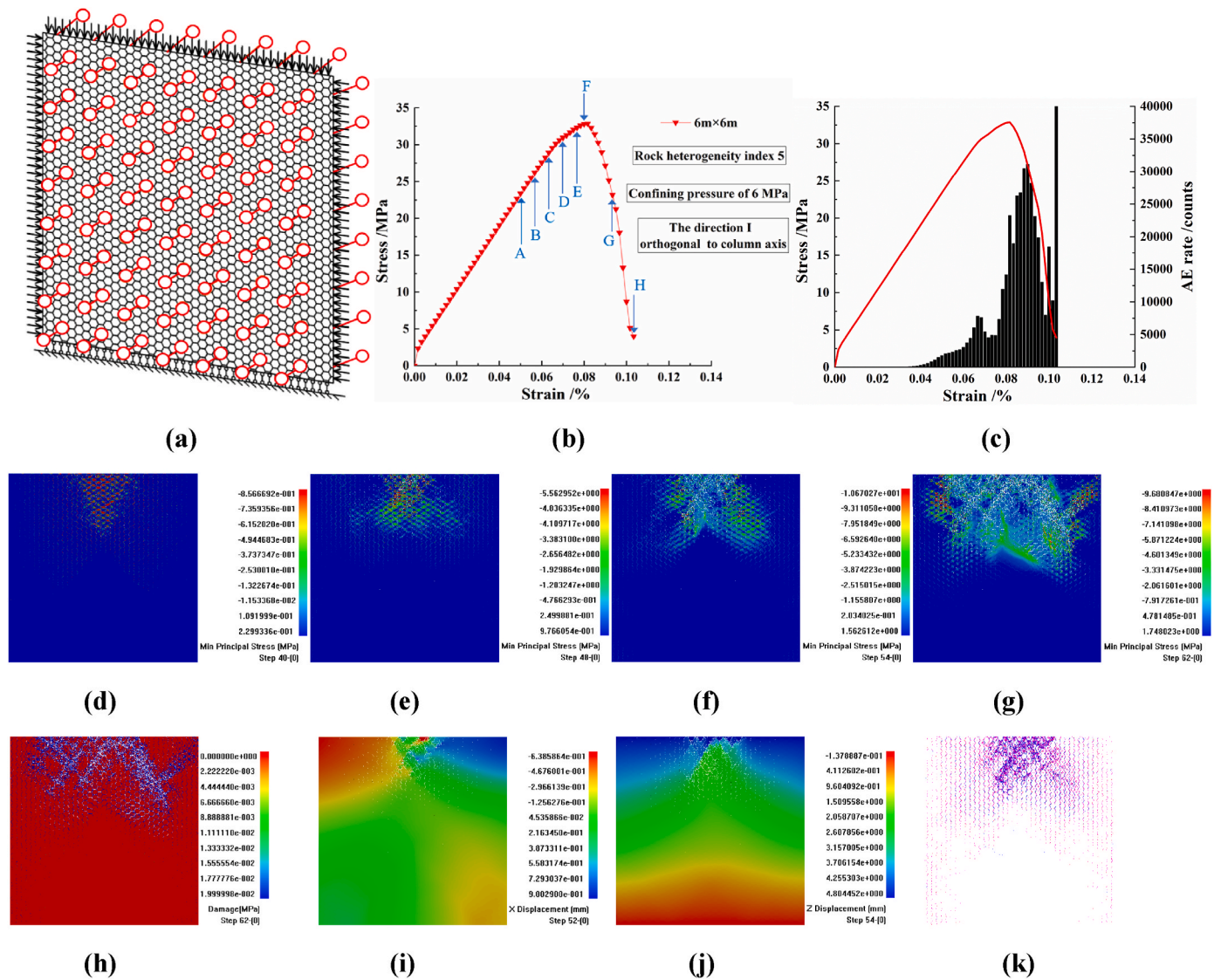


Fig. 9. The progressive failure process and failure pattern along the direction I orthogonal to column axis: (a) the schematic diagram of the CJBs model in the case of plane strain; (b)&(c) the compression stress-strain curve and AE rate; (d)–(g) the minimum principal stress diagrams at Points B, D, F and G corresponding to the stress-strain curve; (h) the damage diagram; (i) the displacement diagram along the x direction; (j) the displacement diagram along the z direction; (k) the AE diagram. (the 6 m specimen with column diameter of 20 cm, heterogeneity index 5, lateral pressure of 6 MPa).

AEs at several column edges (the compression failure is marked in pink AE; the tension failure is marked in blue AE).

3.3. Analysis of influencing factors on size effect and lateral pressure effect of CJBs

3.3.1. Influence of model boundary on size effect and lateral pressure effect of CJBs

As shown in Fig. 12 (a), for the direction parallel to column axis, compared with the model boundary I (the case between plane stress and plane strain, lateral pressure of 0 MPa), for the model boundary III (the case of plane strain, lateral pressure of 0 MPa), the CS of the 3 m specimen increases by 1.93%, and that of the 6 m specimen grows by 2.42%. Compared with the model boundary II (the case between plane stress and plane strain, lateral pressure of 6 MPa), for the model boundary IV (the case of plane strain, lateral pressure of 6 MPa), the CS of the 3 m specimen increases by 7.44%, while that of the 6 m specimen grows by -4.46%.

As presented in Fig. 12 (b), in the aspect of EDM, compared with the model boundary I (the case between plane stress and plane strain, lateral

pressure of 0 MPa), for the model boundary III (the case of plane strain, lateral pressure of 0 MPa), the EDM of the 3 m specimen increases by 1.92%, and that of the 6 m specimen grows by 2.45%. Compared with the model boundary II (the case between plane stress and plane strain, lateral pressure of 6 MPa), for the model boundary IV (the case of plane strain, lateral pressure of 6 MPa), the EDM of the 3 m specimen increases by 4.93%, and that of the 6 m specimen grows by 2.41%.

The model boundaries I, II, III and IV respectively correspond to four kinds of model boundaries: the case between plane stress and plane strain, with lateral pressure of 0 MPa; the case between plane stress and plane strain, with lateral pressure of 6 MPa; the case of plane strain, with lateral pressure of 0 MPa; the case of plane strain, lateral pressure of 6 MPa. Fig. 12 (c)–(f) display the schematic diagrams of the 3 m × 3 m CJBs with $\beta = 30^\circ$ and model boundaries I, II, III and IV, respectively. Fig. 12 (g)–(j) show the schematic diagrams of the 6 m × 6 m CJBs with $\beta = 30^\circ$ and model boundaries I, II, III and IV, respectively. Fig. 12 (k)–(n) are the minimum principal stress diagrams corresponding to Fig. 12 (c)–(f), respectively. Fig. 12 (o)–(r) are the minimum principal stress diagrams corresponding to Fig. 12 (g)–(j), respectively. According to Fig. 12 (k) & (o), for the 3 m × 3 m CJBs with $\beta = 30^\circ$ and model

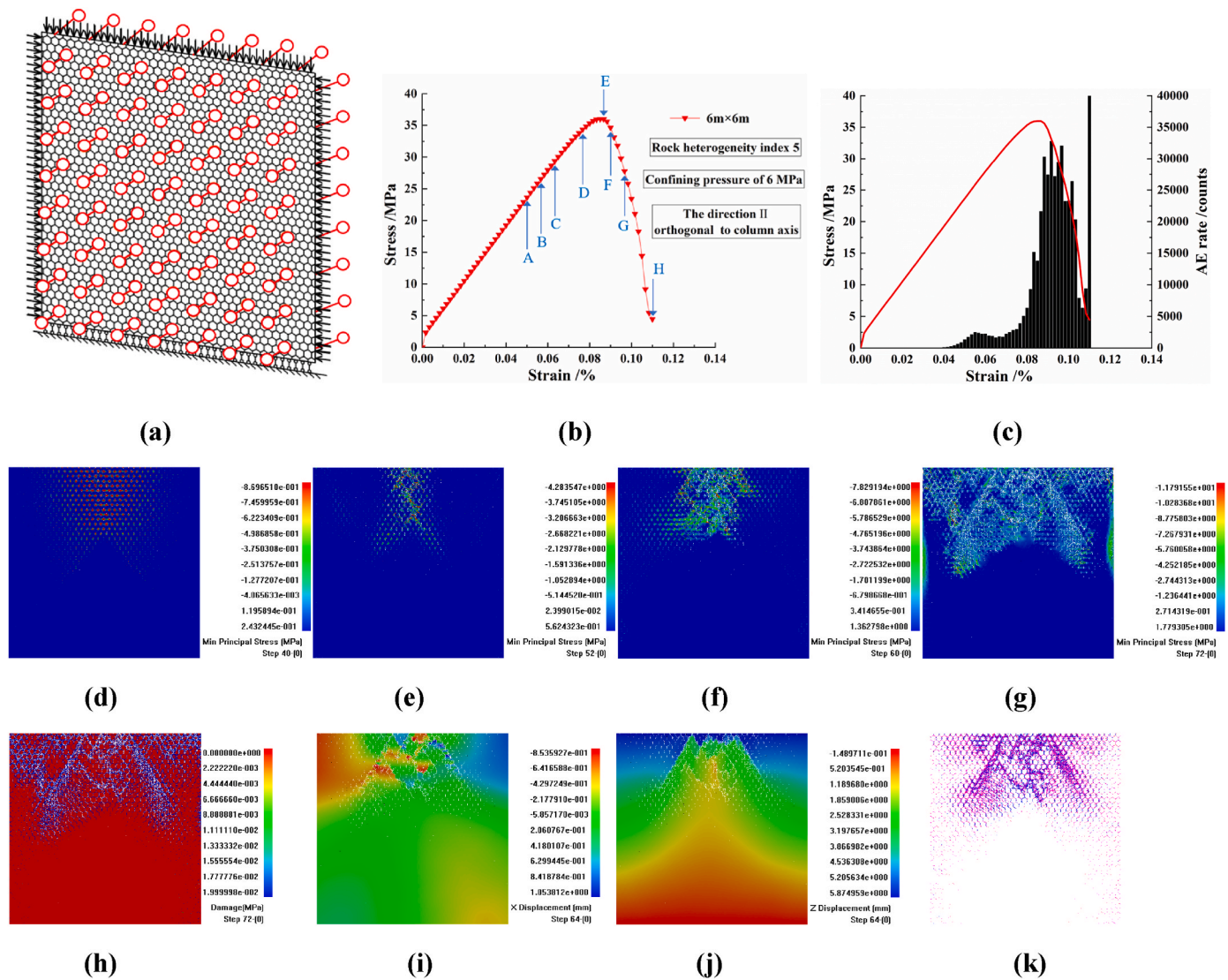


Fig. 10. The progressive failure process and failure pattern along the direction II orthogonal to column axis: (a) the schematic diagram of the CJBs model in the case of plane strain; (b)&(c) the compression stress-strain curve and AE rate; (d)~(g) the minimum principal stress diagrams at Points B, D, F and H corresponding to the stress-strain curve; (h) the damage diagram; (i) the displacement diagram along the x direction; (j) the displacement diagram along the z direction; (k) the AE diagram. (the 6 m specimen with column diameter of 20 cm, heterogeneity index 5, lateral pressure of 6 MPa).

boundary I, at the top of the specimen and near the middle of the specimen, the cracks initiate and propagate, and the stresses concentrate at the crack tips. When the model size is $6\text{ m} \times 6\text{ m}$, at the left and right sides of the upper part of the specimen, crack initiation and propagation occur, and there are stress concentrations at the crack tips. In addition, stress concentrations also appear at the edges of several columns at the left side of the bottom of the specimen. As presented in Fig. 12 (l) & (p), for the $3\text{ m} \times 3\text{ m}$ CJBs with model boundary II, at the top of the specimen and at the upper part of the specimen, there is a crushing zone, respectively. In addition, there is an obvious stress concentration at the position between the middle and the top of the specimen. When the model size is $6\text{ m} \times 6\text{ m}$, at the upper part of the specimen, two strip stress concentration zones are formed, and the fracture is developed at the upper ends within the strip areas. As depicted in Fig. 12 (m) & (q), for the $3\text{ m} \times 3\text{ m}$ CJBs with model boundary III, at the top of the specimen and the middle and upper part of the specimen, there are many stress concentrations and cracks initiate and propagate. When the model size is $6\text{ m} \times 6\text{ m}$, at the upper part of the specimen and the left side of the lower part of the specimen, there are two stress concentration zones, respectively, in which cracks initiate and propagate. As shown in Fig. 12

(n) & (r), for the $3\text{ m} \times 3\text{ m}$ CJBs with model boundary IV, two fracture zones are formed at the upper part of the specimen. When the model size is $6\text{ m} \times 6\text{ m}$, at the upper part of the specimen, the two stress concentration zones are weak, but the crushing phenomenon is obvious within the upper ends of the strip areas.

3.3.2. Influence of elastic modulus of joint on size effect and lateral pressure effect of CJBs

As depicted in Fig. 13 (a)&(c), in terms of CS, for the direction I, the lateral pressure of 0 MPa, under conditions of different elastic moduli of joint, the CS of specimen changes gently with the growth of specimen size; under the lateral pressure of 6 MPa and different elastic moduli of joint, the CS of specimen firstly decreases and then changes gently with the increase of specimen size, and the critical value of size effect is 6 m. For the direction II, under conditions of different elastic moduli of joint, the CS of specimen changes gently with the growth of specimen size; under the lateral pressure of 6 MPa and different elastic moduli of joint, the CS of specimen firstly reduces and then changes gently with the increase of specimen size. For the elastic modulus of 7.5 GPa of joint, the critical value of size effect is 4 m; for the elastic modulus of 15 GPa and

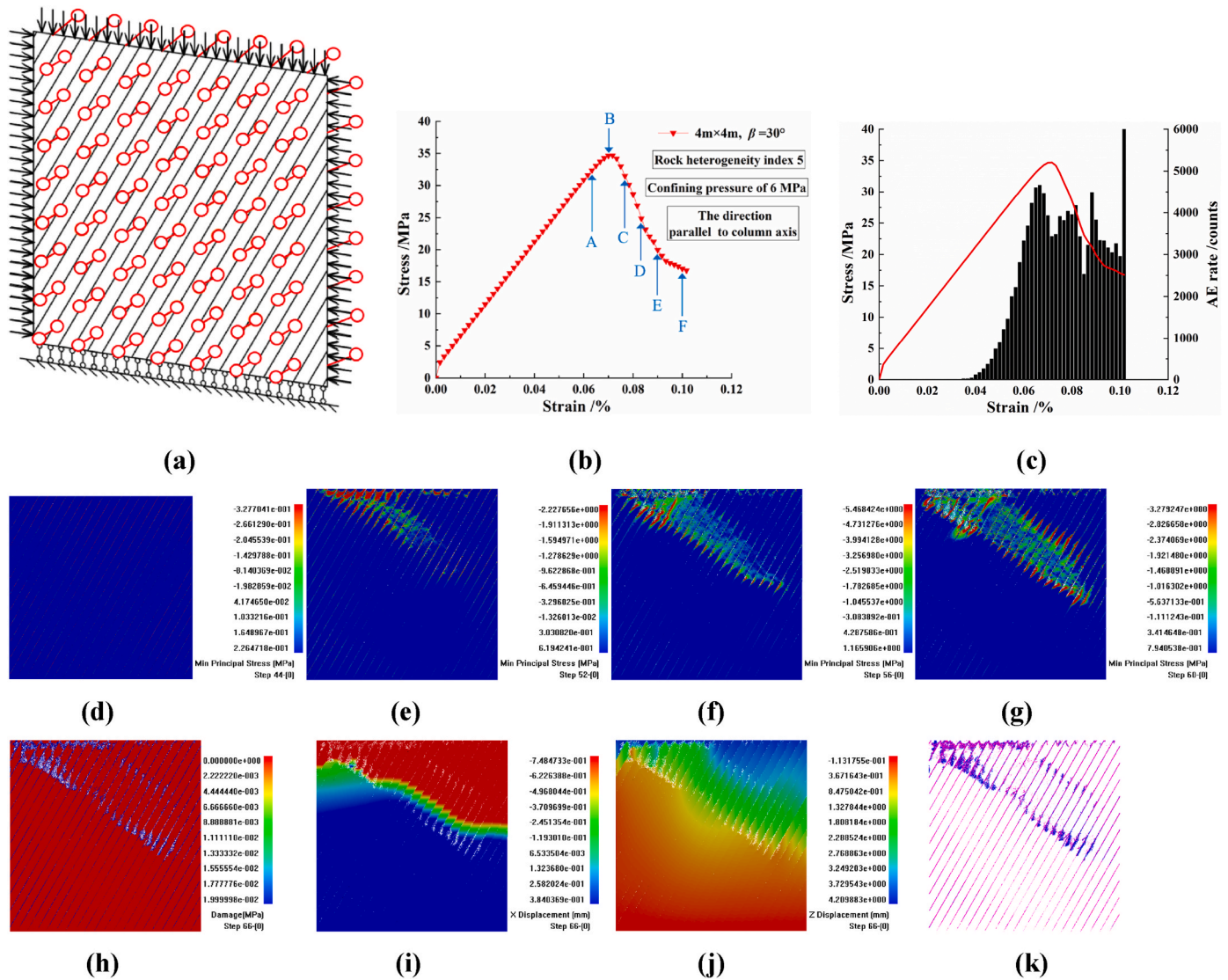


Fig. 11. The progressive failure process and failure pattern along the direction parallel to column axis: (a) the schematic diagram of the CJBs model in the case of plane strain; (b)&(c) the compression stress-strain curve and AE rate; (d)–(g) the minimum principal stress diagrams at points A, C, D and E corresponding to the stress-strain curve; (h) the damage diagram; (i) the displacement diagram along the x direction; (j) the displacement diagram along the z direction; (k) the AE diagram. (the 4 m specimen with $\beta = 30^\circ$, column diameter of 20 cm and heterogeneity index 5, lateral pressure of 6 MPa).

22.5 GPa of joint, the critical value of size effect is 6 m.

As shown in Fig. 13 (b)&(d), in the aspect of EDM, for the direction I, lateral pressures of 0 MPa, 6 MPa, conditions of different elastic moduli of joint, the EDM of specimen roughly increases firstly and then changes gently with the growth of specimen size. For the direction II, lateral pressures of 0 MPa, 6 MPa, conditions of different elastic moduli of joint, the EDM of specimen roughly decreases firstly and then changes gently with the increase of specimen size.

As presented in Fig. 13 (e), in terms of CS, for the lateral pressure of 6 MPa, the direction of specimen parallel to column axis and $\beta = 30^\circ$, with the increase of elastic modulus of joint, the CS of 2 m specimen and 4 m specimen grows gradually. In the aspect of EDM, with the growth of elastic modulus of joint, the EDM of 2 m specimen and 4 m specimen increases rapidly and then grows slowly. When elastic modulus of joint exceeds 15 GPa, the difference of EDMs between the two specimen sizes is small.

3.3.3. Influence of the distance ratio of the secondary joint set on size effect and lateral pressure effect of CJBs

It can be seen from Fig. 14 (a) that in terms of CS, for the direction

parallel to column axis, when the lateral pressure is 0 MPa, the specimen size is 3 m and 6 m, and the distance ratio of the secondary joint set is 0% and 50%, the CS of specimen changes in a U-shape way with the increase of column dip angle; in the case of column dip angles of 60° and 75° , the CSs of specimens with the distance ratio of 50% are larger. When the lateral pressure is 6 MPa, the specimen size is 3 m, and the distance ratio of the secondary joint set is 0% and 50%, the CS of specimen changes in a U-shape way with the growth of column dip angle; in the case of column dip angle of 60° , the CS of the specimen with the distance ratio of 50% is higher. For the 6 m specimens with the distance ratios of 0% and 50%, the CS changes roughly in V-shape with the increase of column dip angle.

As depicted in Fig. 14 (b), in terms of EDM, for the direction parallel to column axis, when the lateral pressure is 0 MPa and 6 MPa, the specimen size is 3 m, and the distance ratio of the secondary joint set is 0% and 50%, the EDM roughly reduces firstly and then changes with the increase of column dip angle. When the lateral pressure is 0 MPa, the specimen size is 6 m, the distance ratio is 0% and 50%, the EDM decreases in fluctuation way with the growth of column dip angle; when the lateral pressure is 6 MPa, the specimen size is 6 m, and the distance

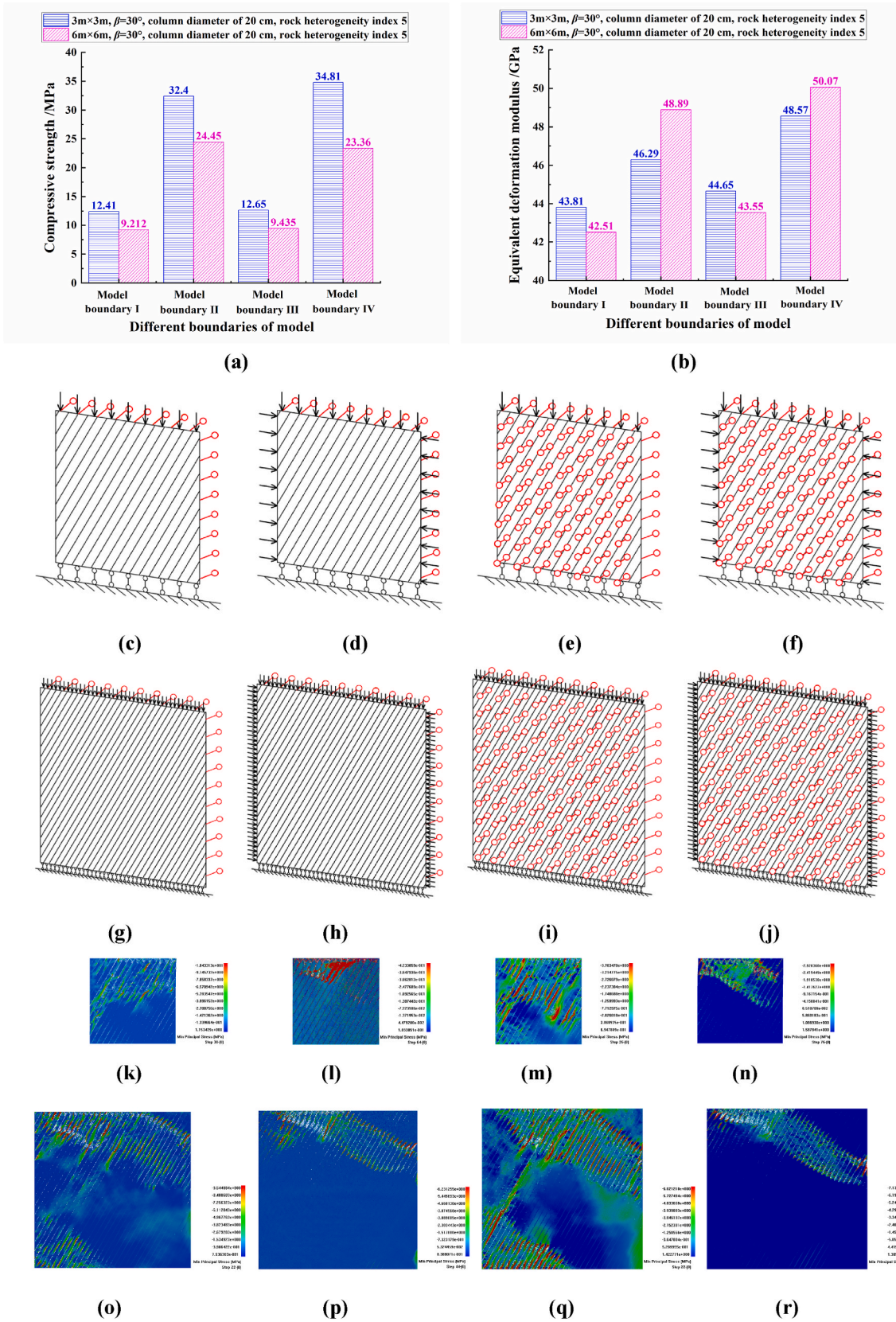
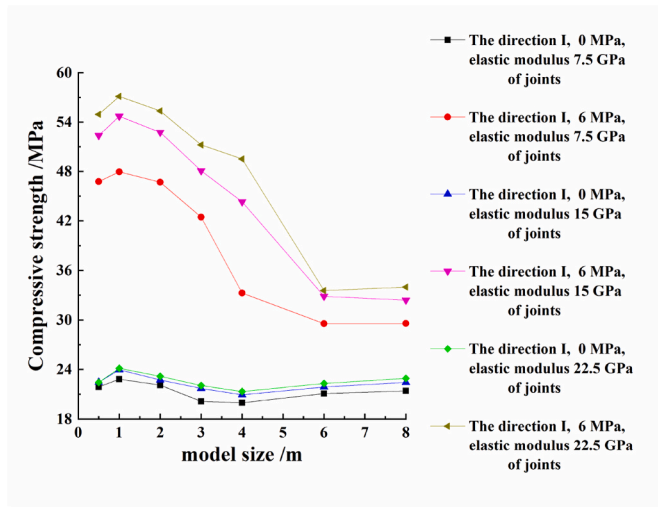
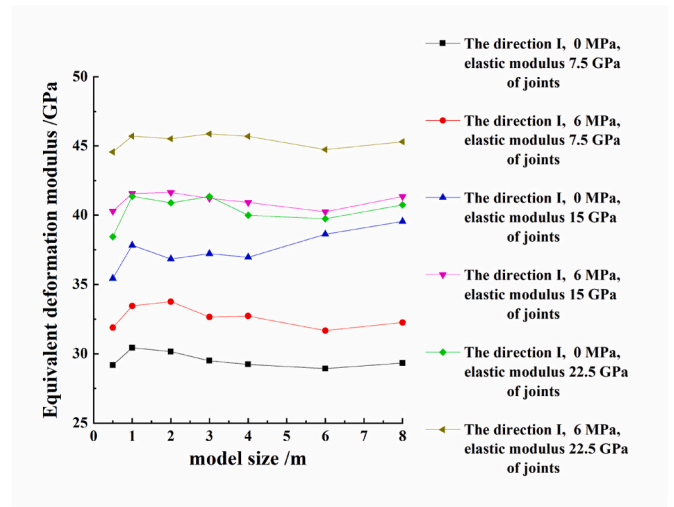


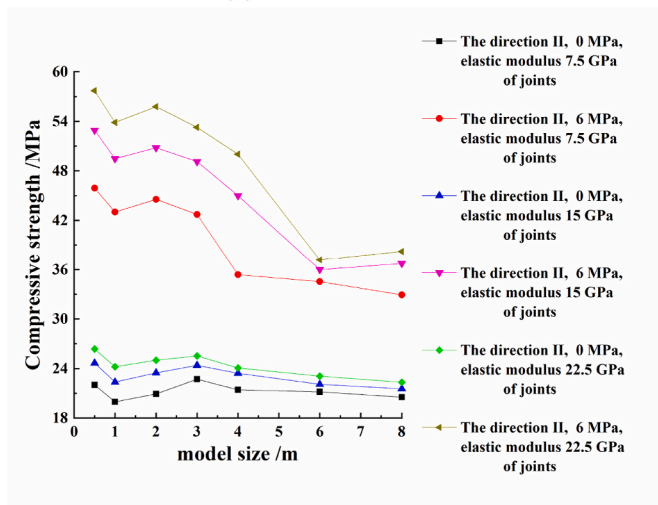
Fig. 12. (a)&(b) The CSs and EDMs of the specimens with different model boundaries along the direction parallel to column axis; (c)~(f) the schematic diagrams of the 3 m CJBs with $\beta = 30^\circ$ and model boundaries I, II, III and IV, respectively; (g)~(j) the schematic diagrams of the 6 m CJBs with model boundaries I, II, III and IV, respectively; (k)~(n) the minimum principal stress diagrams corresponding to the CJBs in (c)~(f); (o)~(r) the minimum principal stress diagrams corresponding to the CJBs in (g)~(j). (the rock heterogeneity index 5).



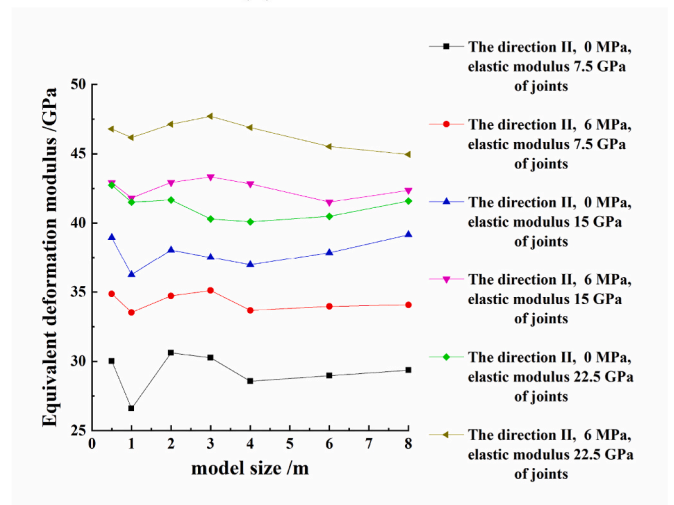
(a)



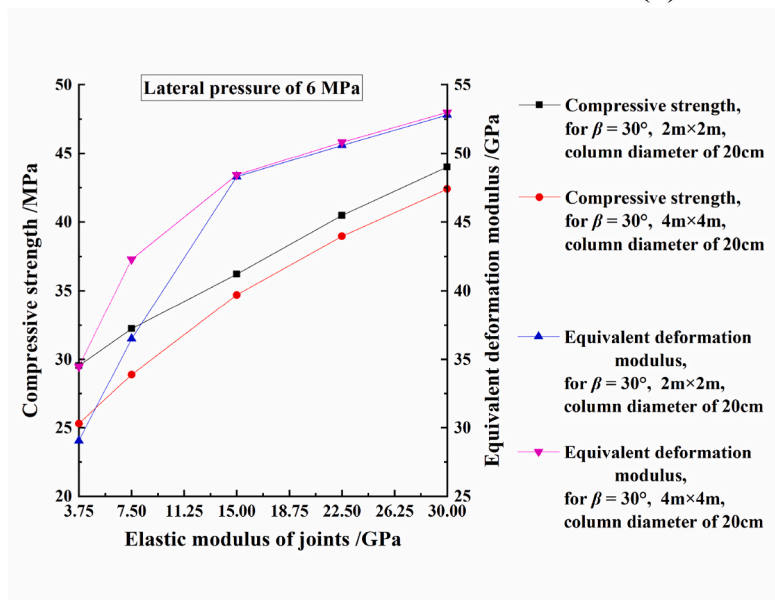
(b)



(c)



(d)



(e)

Fig. 13. (a)&(b)&(c)&(d) The CSs and EDMs of the specimens with different elastic moduli of joint along the directions I & II orthogonal to column axis; (e) the specimens with different elastic moduli of joint along the direction parallel to column axis (the rock heterogeneity index 5).

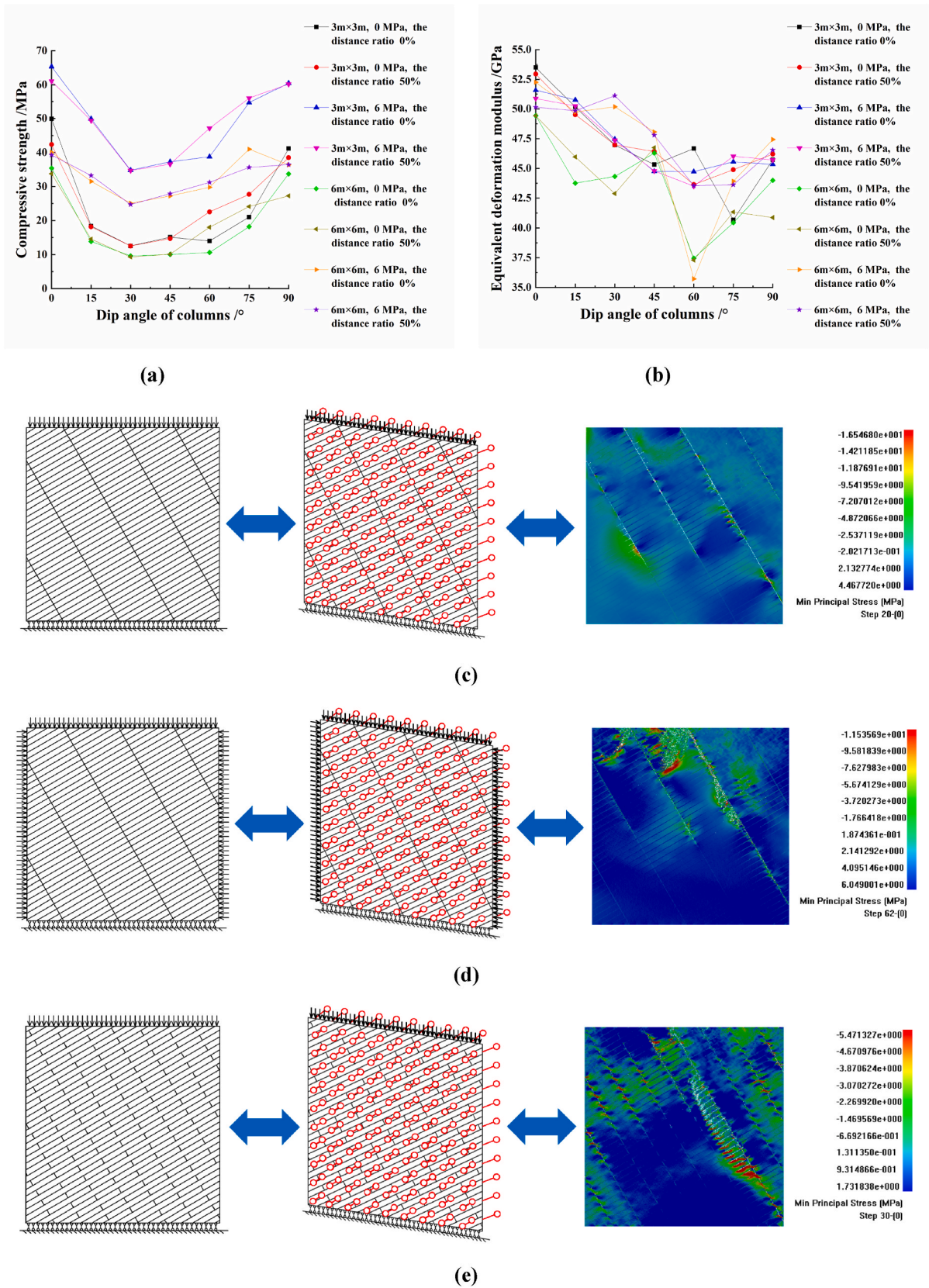


Fig. 14. (a)&(b) The CSs and EDMs of the specimens with different distance ratios of the secondary joint set along the direction parallel to column axis; (c)&(d) the 6 m specimen with $\beta = 60^\circ$ and distance ratio 0% under lateral pressures of 0 MPa & 6 MPa; (e)&(f) the 6 m specimen with $\beta = 60^\circ$ and distance ratio 50% under lateral pressures of 0 MPa & 6 MPa; (g) the specimens with different residual strength coefficients of rock along the directions I & II orthogonal to column axis; (h) the specimens with different residual strength coefficients of rock along the direction parallel to column axis (the rock heterogeneity index 5).

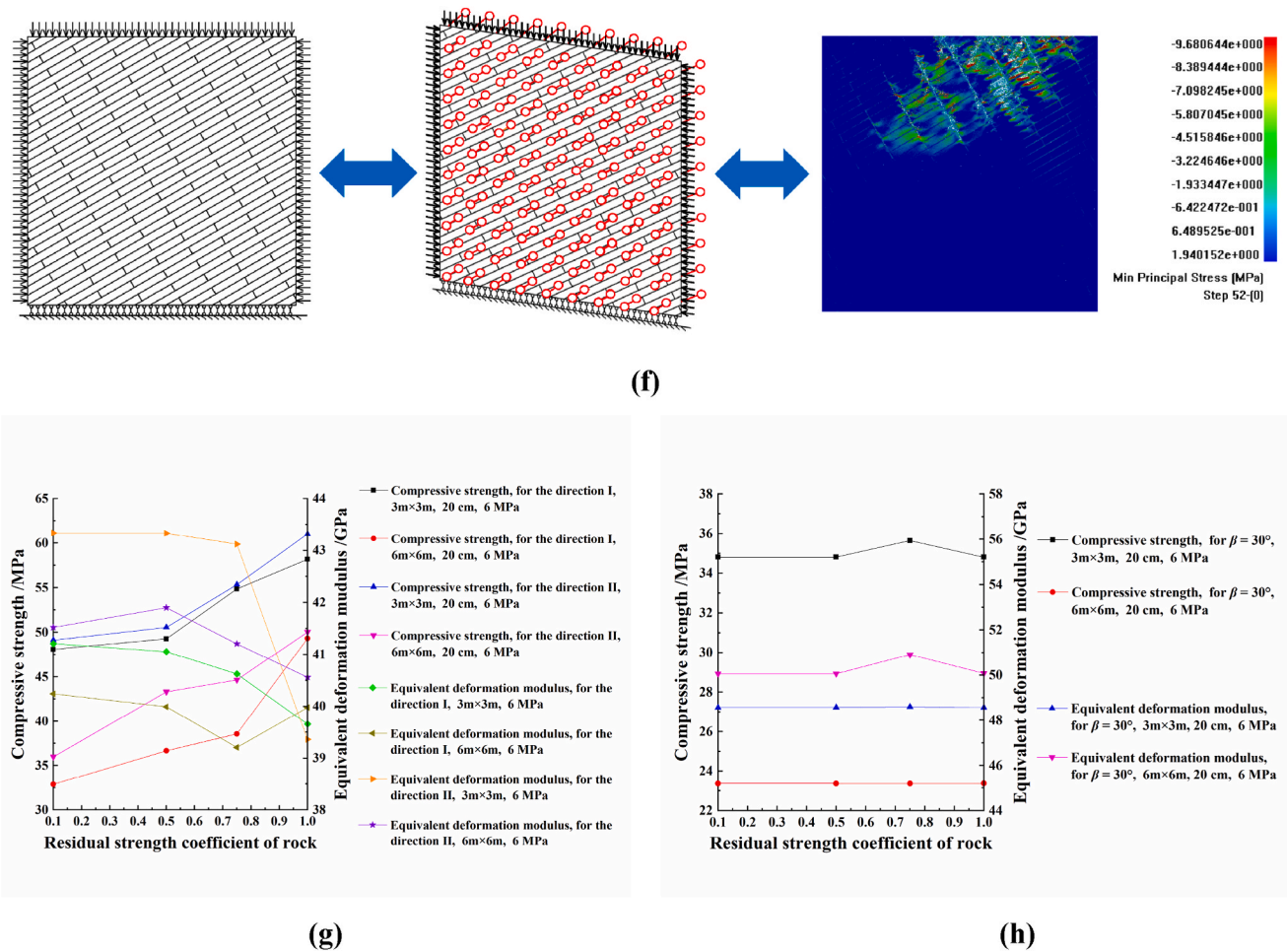


Fig. 14. (continued).

ratio is 0%, the EDM firstly reduces and then grows; when the lateral pressure is 6 MPa, the specimen size is 6 m, and the distance ratio is 50%, the EDM changes gently at first, then decreases, and then changes again with the increase of column dip angle.

Fig. 14 (c)&(d) display the schematic diagrams and the minimum principal stress diagrams for the 6 m × 6 m CJBs with $\beta = 60^\circ$ and the distance ratio 0% of the secondary joint set, under lateral pressures of 0 MPa & 6 MPa, respectively. According to Fig. 14 (c)&(d), under the lateral pressure of 0 MPa, slip cracking occurs at the position of the secondary joint set of the specimen. In addition, weak slip cracking appears at the local area of the primary joint set near the secondary joint set. Under the lateral pressure of 6 MPa, compression shear slip occurs at the secondary joint set of the specimen. Moreover, at the top of the specimen, the shear fracture zones are formed, and at the right side of the specimen, the cracks appear near the secondary joint set.

Fig. 14 (e)&(f) show the schematic diagrams and the minimum principal stress diagrams for the 6 m × 6 m CJBs with $\beta = 60^\circ$ and the distance ratio 50% of the secondary joint set, under lateral pressures of 0 MPa & 6 MPa, respectively. As presented in Fig. 14 (e)&(f), under the lateral pressure of 0 MPa, at the left and right sides of the specimen, the secondary joint set gets cracked, and then the stresses are concentrated near the secondary joint set. Near the middle of the specimen, the secondary joint set is cracked and then shear cracks appear. Then, the primary joint sets between the secondary joint sets get slipped and cracked, and crack initiation and propagation appear at the columns, with the stress concentrations at the crack tips. Under the lateral pressure of 6 MPa, near the middle of the upper part of the specimen, the shear fractures develop at the secondary joint set, and then cracks

initiate and propagate at the columns between the secondary joint sets, and the stresses are concentrated at the crack tips.

3.3.4. Influence of rock meso constitutive relation on size effect and lateral pressure effect of CJBs

As depicted in Fig. 14 (g), in terms of CS, for the direction I, when the lateral pressure is 6 MPa and the specimen size is 3 m and 6 m, the CS grows slowly and then sharply with the increase of residual strength coefficient of rock. For the direction II, when the lateral pressure is 6 MPa and the specimen size is 3 m, the CS increases slowly and then sharply with the growth of residual strength coefficient of rock; the CS of 6 m specimen grows gradually with the increase of residual strength coefficient of rock.

In the aspect of EDM, for the case of the direction I, when the lateral pressure is 6 MPa and the specimen size is 3 m, the EDM reduces gradually with the growth of residual strength coefficient of rock; the EDM of the 6 m specimen decreases firstly and then increases. For the case of the direction II, when the lateral pressure is 6 MPa and the specimen size is 3 m, the EDM changes gently firstly and then reduces sharply with the increase of residual strength coefficient of rock; the EDM of the 6 m specimen increases firstly and then decreases.

As presented in Fig. 14 (h), in terms of CS, for the direction parallel to column axis and $\beta = 30^\circ$, when the lateral pressure is 6 MPa and the specimen size is 3 m and 6 m, the CS changes gently with the growth of residual strength coefficient of rock. In terms of EDM, when the lateral pressure is 6 MPa and the specimen size is 3 m, the EDM changes gently with the increase of residual strength coefficient of rock; for the 6 m specimen, the EDM firstly changes gently, then increases and then

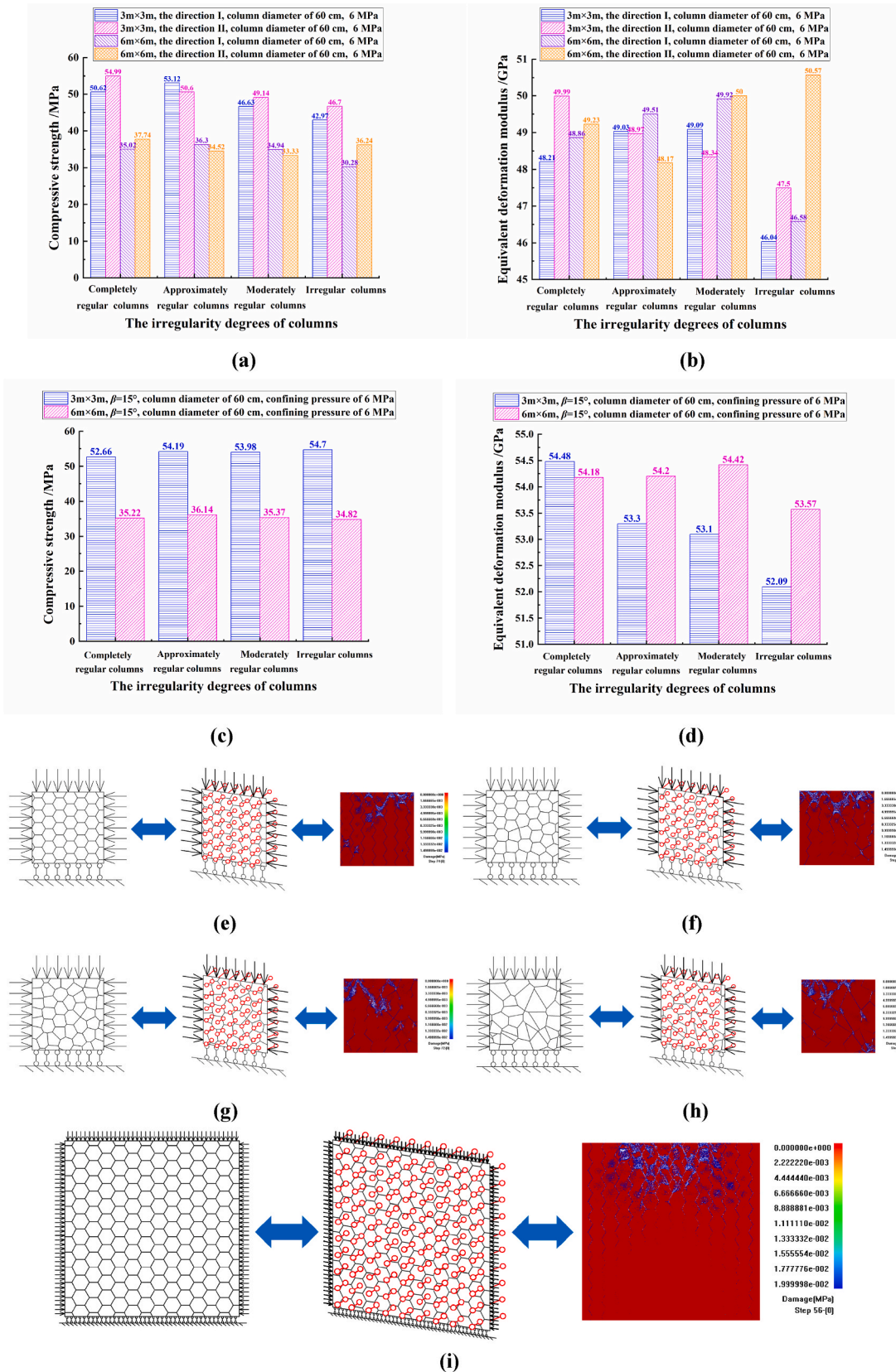


Fig. 15. (a)&(b) The CSs and EDMs of the specimens with different irregularity degrees of columns along the directions I & II orthogonal to column axis; (c)&(d) the specimens with different irregularity degrees of columns along the direction parallel to column axis; (e)&(f)&(g)&(h) for completely regular columns & moderately regular columns & irregular columns, under lateral pressure of 6 MPa, the 3 m specimens with average column diameter 60 cm; (i)&(j)&(k)&(l) for completely regular columns & approximately regular columns & moderately regular columns & irregular columns, under lateral pressure of 6 MPa, the 6 m specimens with average column diameter 60 cm. (the rock heterogeneity index 5).

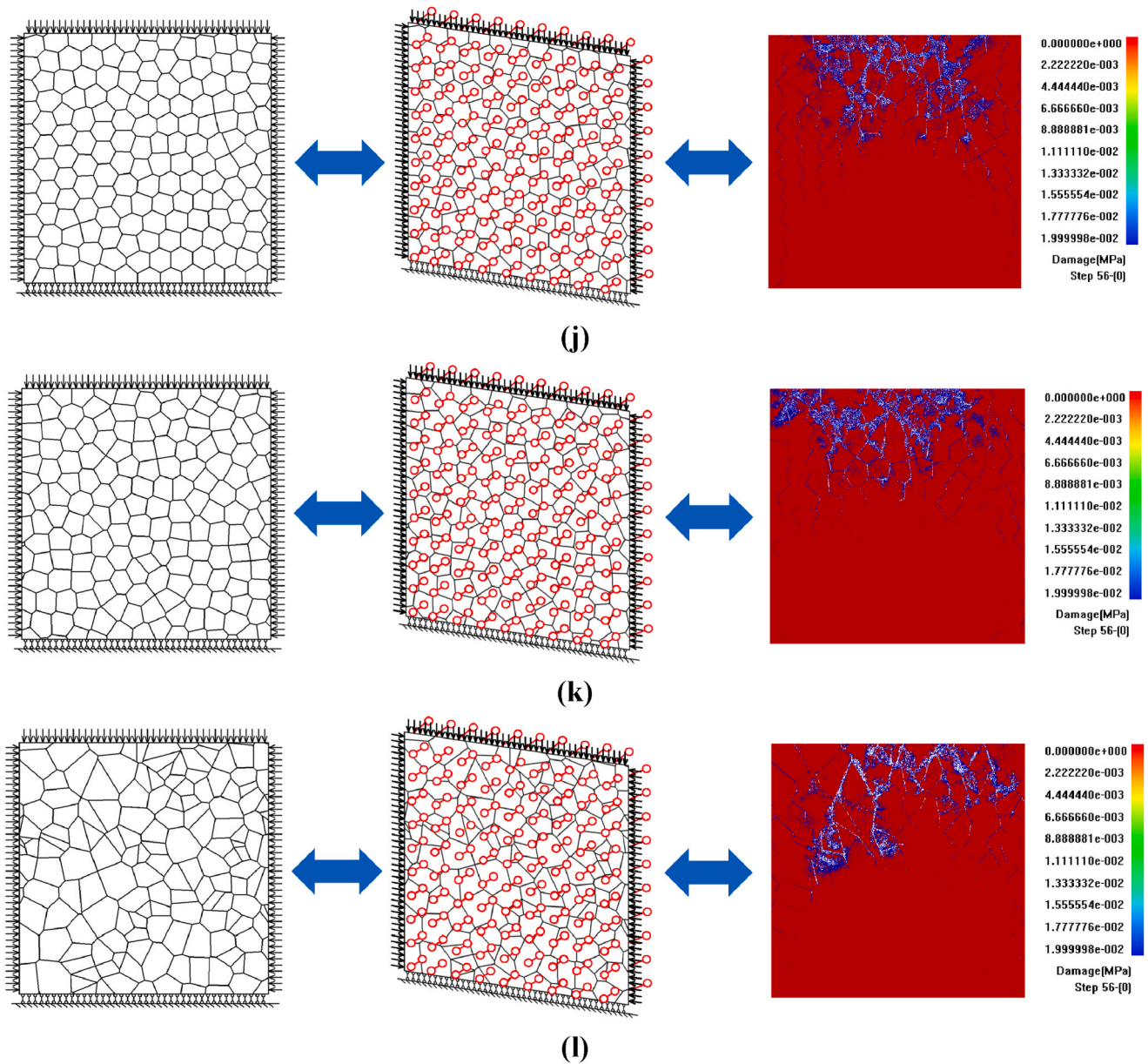


Fig. 15. (continued).

decreases. On the whole, the influence of rock meso constitutive relation on the CS and EDM of the CJBs with $\beta = 30^\circ$ is limited, which is mainly due to the obvious effect of column inclination on the mechanical properties of the CJBs.

3.3.5. Influence of the irregularity degree of columns on size effect and lateral pressure effect of CJBs

It can be seen from Fig. 15 (a) that in terms of CS, for the case of direction I, when the lateral pressure is 6 MPa and the specimen size is 3 m and 6 m, the CS firstly increases and then decreases with the growth of the irregularity degree of columns. For the case of direction II, when the lateral pressure is 6 MPa and the specimen size is 3 m, the CS reduces with the increase of the irregularity degree of columns; the CS of the 6 m specimen firstly decreases and then grows with the growth of the irregularity degree of columns.

As shown in Fig. 15 (b), in the aspect of EDM, for the case of direction I, when the lateral pressure is 6 MPa and the specimen size is 3 m and 6 m, the EDM firstly increases and then decreases with the increase of the irregularity degree of columns. For the case of direction II, when the

lateral pressure is 6 MPa and the specimen size is 3 m, the EDM reduces with the growth of the irregularity degree of columns; when the specimen size is 6 m, the EDM decreases at first and then grows with the increase of the irregularity degree of columns.

As depicted in Fig. 15 (c)&(d), in terms of CS, for the direction parallel to column axis and $\beta = 15^\circ$, when the lateral pressure is 6 MPa and the specimen size is 3 m and 6 m, the CS changes gently with the growth of the irregularity degree of columns. In the aspect of EDM, when the lateral pressure is 6 MPa and the specimen size is 3 m, the EDM decreases with the increase of the irregularity degree of columns; when the specimen size is 6 m, the EDM changes gently and then reduces with the growth of the irregularity degree of columns.

Fig. 15 (e)~(h) show the schematic diagrams and the damage diagrams for the $3\text{ m} \times 3\text{ m}$ CJBs with different irregularity degrees of columns (completely regular columns, approximately regular columns, moderately regular columns, and irregular columns), along the direction I orthogonal to column axis, under lateral pressure of 6 MPa. According to Fig. 15 (e)~(h), in the case of the model size of $3\text{ m} \times 3\text{ m}$, for the CJBs with completely regular column, the vertical joints get damaged at the

upper part of the specimen and the left side of the lower part of the specimen, and the damages are developed at the column sections, and then the fractures initiate and grow. When the columns are approximately regular, the damages appear and the columns are broken near the top of the specimen. In addition, at the right side of the lower part of the specimen, the joint gets fractured due to the extrusion of the columns. For the CJBs with moderately regular columns, at the upper part of the specimen and the right side of the lower part of the specimen, the compression near the corners of the columns is intense, and then the damage fracture zones are formed inside the columns. When the columns are irregular, the joints inside the specimen get damaged and the columns are squeezed against each other. At the middle and upper part of the specimen, the right side of the specimen bottom, the damage fracture zones initiate and develop near the corners of the columns.

Fig. 15 (i)~(l) display the schematic diagrams and the damage diagrams for the 6 m × 6 m CJBs with different irregularity degrees of columns (completely regular columns, approximately regular columns, moderately regular columns, and irregular columns), along the direction I orthogonal to column axis, under lateral pressure of 6 MPa. As presented in Fig. 15 (i)~(l), in the case of the model size of 6 m × 6 m, for the CJBs with completely regular column, at the upper part of the specimen, as well as the left and right sides of the lower part of the specimen, the vertical joints get damaged. Near the middle of the upper part of the specimen, the vertical joints are suffered compression shear and slip cracking, the damages are developed at the column sections, and the fractures initiate and grow. When the columns are approximately regular, at the middle and upper part of the specimen, the damages of joints are developed. Near the middle of the upper part of the specimen, the vertical joints get cracked, the columns are squeezed with each other, and the damage fractures are formed. For the CJBs with moderately regular columns, the damages of joints also appear at the middle and upper part of the specimen. Additionally, at the middle of the upper part of the specimen, the vertical joints are cracked, and further, the columns are compressed to form damage fractures. When the columns are irregular, at the middle and upper part of the specimen, the joints are damaged. Moreover, at the middle of the upper part of the specimen, the vertical joints get cracked, the oblique joints are compressed, sheared and slipped, and the damage fractures develop near the corners of the columns.

4. Discussion

4.1. Strength characteristics and size effect of CJBs under different lateral pressures

In this paper, for the direction I orthogonal to column axis, in terms of CS, when the lateral pressure is 0 MPa, the CS of specimen changes gently with the increase of model size; when the lateral pressure is 2 MPa and 6 MPa, the CS of specimen firstly decreases and then changes gently with the growth of model size. The critical value of size effect is 4 m when the lateral pressure is 2 MPa, and 6 m when the lateral pressure is 6 MPa. For the direction II orthogonal to column axis, when the lateral pressure is 0 MPa, the CS of specimen changes gently with the increase of model size. When the lateral pressure is 2 MPa, the CS of specimen decreases in a stair way with the growth of model size, and the critical value of size effect is 4 m; when the lateral pressure is 6 MPa, the CS of specimen firstly decreases and then changes gently with the increase of model size, and the critical value of size effect is 6 m.

For the direction parallel to column axis, when the lateral pressure is 6 MPa and the specimen size is 0.5 m, 1 m, 2 m, 3 m and 4 m, the CS of specimen decreases roughly with the growth of specimen size at the column dip angles of 0°–90°. For the case of the lateral pressures of 0 MPa, 2 MPa and 6 MPa and the specimen size of 4 m, the CS of specimen is obviously improved with the increase of lateral pressure at the column dip angles of 0°–90°.

Chong et al.⁴⁴ used the discrete element method to study the

anisotropy and size effect of jointed rock mass. The results showed that when the specimen size increases to a certain extent, the compressive strength of the specimen decreases to a certain range, and the change is not obvious. Lin et al.²⁰ used the physical model test method to study the size effect of columnar jointed rock mass with transverse joints. The results showed that when column dip angle was 0° and 90°, the compressive strength of specimen decreased obviously with the increase of specimen size. However, the loading condition was uniaxial compression, and the influence of lateral pressure has not been further considered. Zhou et al.⁴⁵ used PFC2D software to study the mechanical properties of specimens with single joint and double joints, and the influence of lateral pressure was considered for specimens with single joint, but not for specimens with double joints. Cui et al.⁴⁶ used the discrete fracture network method to study the size effect of jointed rock mass, and also found that when the specimen size increased to a certain extent, the compressive strength of specimen decreased to a relatively stable range, but the influence of rock heterogeneity and lateral pressure on the size effect has not been further considered in their study. Zhou et al.⁴⁷ used the equivalent rock mass technology to carry out the macro and micro analysis of multi-scale jointed rock mass under triaxial compression. The results indicated that the compressive strength of jointed rock mass with different loading directions appeared with obvious differences, while the compressive strength of specimens with different sizes in the same loading direction showed limited differences. Fan et al.⁴⁸ used PFC3D to study the mechanical properties of specimens with multi-non-persistent joints under uniaxial compression, and analyzed the variation of compressive strength with the increase of joint dip angle and joint length. With the increase of joint length, the compressive strength was more sensitive to the change of joint dip angle. Liu et al.⁴⁹ carried out numerical simulation research on the anisotropy and size effect of jointed rock mass. The results showed that under different lateral pressures, the compressive strength of specimen would gradually tend to a stable value with the increase of specimen size. It is consistent with some of the research results in this paper. Cui et al.⁵⁰ studied the structural effect of equivalent elastic modulus of columnar jointed rock mass, and analyzed the influence of distance ratio of joint, joint stiffness, irregularity degree of columns on the equivalent elastic modulus of specimens, but the influence of rock meso constitutive laws and model size effect has not been further considered in their research.

4.2. Influence of elastic modulus of joint on size effect and lateral pressure effect of CJBs

In this paper, for the direction I (II), in terms of CS, under the lateral pressure of 0 MPa and conditions of different elastic moduli of joint, the CS of specimen changes gently with the increase of specimen size; under the lateral pressure of 6 MPa and different elastic moduli of joint, the CS of specimen firstly decreases and then changes gently with the growth of specimen size. In the aspect of EDM, for the direction I, the lateral pressure of 0 MPa, 6 MPa, conditions of different elastic moduli of joint, the EDM of specimen roughly increases firstly and then changes gently with the increase of specimen size. For the direction II, lateral pressure of 0 MPa, 6 MPa, conditions of different elastic moduli of joint, the EDM of specimen roughly decreases firstly and then changes gently with the growth of specimen size.

For the direction parallel to column axis, $\beta = 30^\circ$, and the lateral pressure of 6 MPa, with the increase of elastic modulus of joint, the CS of 2 m specimen and 4 m specimen grows gradually. In the aspect of EDM, with the growth of elastic modulus of joint, the EDM of 2 m specimen and 4 m specimen increases rapidly and then grows slowly. When elastic modulus of joint exceeds 15 GPa, the difference of EDMs between the two specimen sizes is small.

The results of Pariseau et al.⁵¹ showed that with the increase of joint length, the normalized equivalent elastic modulus of jointed layer with non-persistent joint would gradually decrease and tend to a certain stable value; however, with the increase of the number of joint sets, the

normalized REV equivalent elastic modulus or shear modulus would gradually decrease, and the phenomenon of tending to a certain stable value is not obvious. It is different from the research results in this paper, and the reason may be related to the rock mass type. The results of Vallier et al.⁵² showed that in the case of infinitesimal relative shear displacement, with the increase of joint length, the decrease of tangential stiffness of joint is very small; in the case of larger finite shear displacement, with the increase of joint length, the tangential stiffness of joint decreases relatively obviously. Zheng et al.⁵³ conducted shear tests on granite jointed specimens. The results showed that the peak shear strength increases with the increase of normal stress or serration angle. Lin et al.⁵⁴ showed that the shear stiffness of specimen increases roughly with the increase of normal stress. The above researches mainly focus on the influences of changes of shear mode, normal stress and sawtooth angle on the mechanical properties of joints. The research in this paper is to study the influence of the change of mechanical properties of joints on the CJBs under lateral pressure. Wang et al.⁵⁵ used PFC software to carry out numerical tests on the specimens without considering the joint roughness morphology and the specimens with considering the joint roughness morphology. The results showed that, compared with the specimens without considering the joint roughness morphology, the specimens with considering the joint roughness morphology had higher tangential stiffness and peak shear strength; with the increase of specimen size, the peak shear strength of the former decreased gradually, and the peak shear strength of the latter decreased in fluctuation way firstly and then increased slowly. The above research results are similar with some of the research results in this paper, that is, for different joint elastic moduli, the compressive strength decreases with the increase of specimen size. The research of Fardin et al.⁵⁶ showed that with the increase of rock joint surface size, the roughness coefficient of joint surface gradually decreased to a certain stable value. In this paper, the effect of joint mechanical properties on the compressive strength and equivalent deformation modulus of the CJBs is mainly considered.

4.3. Influence of constitutive relation of rock on size effect and lateral pressure effect of CJBs

In this paper, for the direction I, in terms of CS, when the lateral pressure is 6 MPa and the specimen size is 3 m and 6 m, the CS increases slowly and then sharply with the growth of residual strength coefficient of rock. For the direction II, when the lateral pressure is 6 MPa and the specimen size is 3 m, the CS grows slowly and then sharply with the increase of residual strength coefficient of rock; the CS of 6 m specimen grows gradually with the increase of residual strength coefficient of rock.

For the direction parallel to column axis and $\beta = 30^\circ$, in terms of CS, when the lateral pressure is 6 MPa and the specimen size is 3 m and 6 m, the CS changes gently with the increase of residual strength coefficient of rock. In terms of EDM, when the lateral pressure is 6 MPa and the specimen size is 3 m, the EDM changes gently with the growth of residual strength coefficient of rock; for the 6 m specimen, the EDM firstly changes gently, then increases and then decreases.

The research of Niazmandi et al.⁵⁷ showed that different types of compression test methods (uniaxial compression, biaxial compression, conventional triaxial compression, true triaxial compression) had different effects on the mechanical behavior of the stress-strain curve of discrete fractured rock mass. When the compression test method changed from uniaxial compression to true triaxial compression, the stress-strain curve of specimen changed from a certain ductile failure to plastic failure and the REV of specimen strength decreased. Liu et al.⁴⁹ showed that the stress-strain curve of jointed rock mass would show ideal elastic-plastic failure characteristics due to shear of joint and rotation of rock block under lateral pressure when the joint dip angle was parallel to the principal shear stress. The above researches mainly focus on the effects of loading mode and loading direction on the mechanical properties of specimens. In this paper, the effect of different

rock meso constitutive models on the CJBs under lateral pressure is studied. Stavrou et al.⁵⁸ used UDEC software to carry out numerical compression tests on two kinds of intact rock specimens (one is the specimen with weak mechanical parameters, the other is the specimen with strong mechanical parameters) under lateral pressure. The results indicated that with the increase of lateral pressure, the stress-strain curve of the former specimen gradually showed the mechanical characteristics from brittle drop to ductile failure, while that of the latter specimen gradually showed the mechanical characteristics from brittle drop, ductile failure to strain hardening. In this paper, the effect of the rock meso constitutive change, from brittle mechanical behavior to plastic mechanical behavior, on the compressive strength and equivalent deformation modulus of the CJBs under the same lateral pressure is considered. Wu et al.⁵⁹ studied fracture tensor, anisotropy and size effect of jointed rock mass, and proposed an orthotropic constitutive model, which was applied to the calculation of dam rock mass. The results showed that the rock mass has obvious anisotropic mechanical characteristics before peak stress. However, in their study, the rock meso heterogeneity is not considered, and the rock mass structure is different from the CJBs in this paper. Yang et al.⁶⁰ used a numerical method of coupling stress-damage-seepage to study the mechanical properties of jointed rock mass under seepage-stress loading. The results indicated that with the increase of specimen size, the stress-strain curve showed the characteristics of transformation from brittle failure to ductile failure. In this paper, the effects of different rock meso constitutive laws and specimen sizes on the mechanical properties of the CJBs are studied. The numerical test results of Wu et al.⁶¹ indicated that with the increase of lateral pressure, the stress-strain curve of jointed rock mass was with obvious ductile failure characteristics. In addition, the jointed rock mass showed different degrees of brittle failure or ductile failure characteristics under different loading directions. In this paper, based on considering the changes of rock meso mechanical properties, the compressive strength and equivalent deformation modulus of the CJBs under lateral pressure are studied.

5. Conclusions

With the aim of revealing the size effect and lateral pressure effect of CJBs, the meso-damage mechanics, statistical strength theory, continuum mechanics and digital image correlation are combined, and a series of heterogeneous numerical models of CJBs orthogonal and parallel to column axis are established. The gradual fracture processes and AE characteristics of CJBs are numerically simulated under lateral pressure. Then the influence factors on the size effect and lateral pressure effect of CJBs are revealed. The main conclusions can be summarized as follows.

- (1) Along the direction I orthogonal to column axis, the progressive fracture process and failure pattern of CJBs are as follows: the vertical joints at the middle of the upper part of specimen get cracked initially. Then the stress concentration is transferred to the column centers at this area, which induces more cracks to initiate and propagate. Meanwhile, with the increase of lateral pressure, the mode of stress concentration inside the specimen is changed at the beginning of loading, the failure region at the upper part of specimen is narrowed at the later stage of loading and the first peak of the AE rate gradually moves to the right.
- (2) Along the direction parallel to column axis, the progressive fracture process and failure pattern of CJBs are as follows: the stress concentration firstly appears at columnar joints inside specimen and then columnar joints are sheared and slid. With the increase of loading, the high stress concentrates at the edges of the columns and leads to more cracks. Moreover, with the increase of lateral pressure, the stress concentration tends to appear at the columnar joints at the initial loading stage. Later, there are two strip regions of stress concentration occurring and resulting in final macro failure.

- (3) For the direction I (II) orthogonal to column axis, when the lateral pressure is 0 MPa, the compressive strength of the specimen changes gently with the model size rising; when the lateral pressure is 2 MPa and 6 MPa, the critical value of size effect is 4 m and 6 m, respectively. For the direction parallel to column axis, when the lateral pressure is 6 MPa, the compressive strength decreases roughly with the specimen size increasing from 0.5 m to 4 m. For the certain specimen size, the compressive strength of specimen can be obviously improved by increasing the lateral pressure.
- (4) For the direction I, when the lateral pressure is 6 MPa and the specimen size is 3 m or 6 m, the compressive strength increases slowly and then sharply with the residual strength coefficient of rock increasing. For the direction II, when the lateral pressure is 6 MPa and the specimen size is 3 m, the compressive strength shows the same trend, but the compressive strength of 6 m specimen increases gradually with the growth of residual strength coefficient of rock. Simultaneously, for the direction parallel to column axis and $\beta = 30^\circ$, when the lateral pressure is 6 MPa and the specimen size is 3 m or 6 m, the compression strength and equivalent deformation modulus fluctuate gently with the increase of residual strength coefficient of rock, indicating the influence of rock meso constitutive relation on the CS and EDM of the CJBs with $\beta = 30^\circ$ is limited, which is mainly due to the obvious effect of column inclination on the mechanical properties of the CJBs.
- (5) For the direction parallel to column axis, when the lateral pressure is 0 MPa, the specimen size is 3 m and 6 m, and the distance ratio of the secondary joint set is 0% and 50%, the compression strength of specimen changes in a U-shape trend with the increase of column dip angle. When the lateral pressure is 6 MPa, the compression strength of the 3 m specimen shows the same trend, but it changes roughly in V-shape trend with the increase of column dip angle for the 6 m specimen.
- (6) By revealing the deformation characteristics, progressive fracture processes, strengths, failure patterns of CJBs affected by the size effect and lateral pressure effect, the achievements can provide the theoretical basis for utilizing both experimental and field test data and contribute to the stability assessment and safe design of rock structures when CJBs are encountered, such as dams, slopes and tunnels.

Declaration of competing interest

The authors declare that they have no known competing financial interests or personal relationships that could have appeared to influence the work reported in this paper.

Data availability

Data will be made available on request.

Acknowledgements

This study was financially supported by the National Natural Science Foundation of China (Grant Nos. 42102314 and 42050201), the National Basic Research Program of China (Grant No. 2018YFC1505301), and the China Postdoctoral Science Foundation (Grant No. 2020M680950), for which the authors are very grateful.

References

- 1 Jiang Q, Wang B, Feng XT, et al. In situ failure investigation and time-dependent damage test for columnar jointed basalt at the Baihetan left dam foundation. *Bull Eng Geol Environ.* 2019;78:3875–3890.
- 2 Ke ZQ, Wang HL, Xu WY, Lin ZN, Ji H. Experimental study of mechanical behaviour of artificial columnar jointed rock mass containing transverse joints. *Rock Soil Mech.* 2019;40(2):660–667.
- 3 Lin ZN, Xu WY, Wang HL, et al. Anisotropic characteristic of irregular columnar-jointed rock mass based on physical model test. *KSCE J Civ Eng.* 2017;21(5):1728–1734.
- 4 Que XC, Zhu ZD, Niu ZH, Lu WN. Estimating the strength and deformation of columnar jointed rock mass based on physical model test. *Bull Eng Geol Environ.* 2021;80(2):1557–1570.
- 5 Zou LF, Xu WY, Meng GT, Ning Y, Wang HL. Permeability anisotropy of columnar jointed rock masses. *KSCE J Civ Eng.* 2018;22(10):3802–3809.
- 6 Meng QX, Wang HL, Xu WY, Chen YL. Numerical homogenization study on the effects of columnar jointed structure on the mechanical properties of rock mass. *Int J Rock Mech Min Sci.* 2019;124, 104127.
- 7 Xiang ZP, Wang HL, Xu WY, Xie WC. Experimental study on hydro-mechanical behaviour of anisotropic columnar jointed rock-like specimens. *Rock Mech Rock Eng.* 2020;53(12):5781–5794.
- 8 Weinberger R, Burg A. Reappraising columnar joints in different rock types and settings. *J Struct Geol.* 2019;125:185–194.
- 9 Xu SS, Nieto-Samaniego AF, Alaniz-Alvarez SA. Column-normal fracture features of the basaltic joints in Santa Maria Regla, Hidalgo state, Mexico. *J. South Am. Earth Sci.* 2020;101, 102611.
- 10 Sarfarazi V, Haeri H, Shemirani AB. The effect of compression load and rock bridge geometry on the shear mechanism of weak plane. *Geomech. Eng.* 2017;13(3):431–446.
- 11 Haeri H, Sarfarazi V, Zhu Z, Moosavi E. Effect of transversely bedding layer on the biaxial failure mechanism of brittle materials. *Struct Eng Mech.* 2019;69(1):11–20.
- 12 Sarfarazi V, Haeri H, Ebneabbasi P, Bagheri K. Simulation of the tensile behaviour of layered anisotropy rocks consisting internal notch. *Struct Eng Mech.* 2019;69(1):51–67.
- 13 Meng G, Detournay C, Peter Cundall. Formulation and application of a constitutive model for multijointed material to rock mass engineering. *Int J GeoMech.* 2020;20, 04020044.
- 14 Hao XJ, Feng XT, Yang CX, Jiang Q, Li SJ. Analysis of EDZ development of columnar jointed rock mass in the Baihetan diversion tunnel. *Rock Mech Rock Eng.* 2016;49(4):1289–1312.
- 15 Xiao YX, Feng XT, Chen BR, Feng GL, Yao ZB, Hu LX. Excavation-induced microseismicity in the columnar jointed basalt of an underground hydropower station. *Int J Rock Mech Min Sci.* 2017;97:99–109.
- 16 Jiang Q, Feng XT, Hatzor YH, Hao XJ, Li SJ. Mechanical anisotropy of columnar jointed basalts: an example from the Baihetan hydropower station, China. *Eng Geol.* 2014;175:35–45.
- 17 Chen BR, Li QP, Feng XT, Xiao YX, Feng GL, Hu LX. Microseismic monitoring of columnar jointed basalt fracture activity: a trial at the Baihetan hydropower station, China. *J Seismol.* 2014;18(4):773–793.
- 18 Feng XT, Hao XJ, Jiang Q, Li SJ, Hudson JA. Rock cracking indices for improved tunnel support design: a case study for columnar jointed rock masses. *Rock Mech Rock Eng.* 2016;49(6):2115–2130.
- 19 Jin CY, Li SG, Liu JP. Anisotropic mechanical behaviors of columnar jointed basalt under compression. *Bull Eng Geol Environ.* 2018;77(1):317–330.
- 20 Lin Z, Xu W, Wang W, et al. Determination of strength and deformation properties of columnar jointed rock mass using physical model tests. *KSCE J Civ Eng.* 2018;22(9):3302–3311.
- 21 Ji H, Zhang JC, Xu WY, et al. Experimental investigation of the anisotropic mechanical properties of a columnar jointed rock mass: observations from laboratory-based physical modelling. *Rock Mech Rock Eng.* 2017;50(7):1919–1931.
- 22 Haeri H, Sarfarazi V, Zhu Z. Numerical simulation of the effect of bedding layer geometrical properties on the punch shear test using PFC3D. *Struct Eng Mech.* 2018;68(4):507–517.
- 23 Haeri H, Sarfarazi V, Zhu Z, Nejadi HR. Numerical simulations of fracture shear test in anisotropy rocks with bedding layers. *Adv. Concr. Constr.* 2019;7(4):241–247.
- 24 Haeri H, Sarfarazi V, Zhu Z, Marji MF. Simulation of the tensile failure behaviour of transversally bedding layers using PFC2D. *Struct Eng Mech.* 2018;67(5):493–504.
- 25 Niu ZH, Zhu ZD, Que XC. Constitutive model of stress-dependent seepage in columnar jointed rock mass. *Symmetry-Basel.* 2020;12(1):160.
- 26 Meng QX, Yan L, Chen YL, Zhang Q. Generation of numerical models of anisotropic columnar jointed rock mass using modified centroidal voronoi diagrams. *Symmetry-Basel.* 2018;10(11):618.
- 27 Yan L, Xu WY, Wang RB, Meng QX. Numerical simulation of the anisotropic properties of a columnar jointed rock mass under triaxial compression. *Eng Comput.* 2018;35(4):1788–1804.
- 28 Tang CA. Numerical simulation of progressive rock failure and associated seismicity. *Int J Rock Mech Min Sci.* 1997;34(2):249.
- 29 Liang ZZ. *Three-dimensional Failure Process Analysis of Rock and Associated Numerical Tests.* PhD Thesis. Shenyang China: Northeastern University; 2005.
- 30 Li LC, Yang TH, Liang ZZ, Zhu WC, Tang CN. Numerical investigation of groundwater outbursts near faults in underground coal mines. *Int J Coal Geol.* 2011;85(3-4):276–288.
- 31 Yu QL, Yang TH, Tang SB, et al. The 3D reconstruction method for quasi-brittle material structure and application. *Eng Mech.* 2015;32(11):51–62+114.
- 32 Tang CA, Kou SQ. Crack propagation and coalescence in brittle materials under compression. *Eng Fract Mech.* 1998;61(3-4):311–324.
- 33 Tang CA, Lin P, Wong RHC, Chau KT. Analysis of crack coalescence in rock-like materials containing three flaws-Part II: numerical approach. *Int J Rock Mech Min Sci.* 2001;38(7):925–939.

- 34 Xu T, Ranjith PG, Wasantha PLP, Zhao J, Tang CA, Zhu WC. Influence of the geometry of partially-spanning joints on mechanical properties of rock in uniaxial compression. *Eng Geol.* 2013;167:134–147.
- 35 Li LC, Tang CA, Zhu WC, Liang ZZ. Numerical analysis of slope stability based on the gravity increase method. *Comput Geotech.* 2009;36(7):1246–1258.
- 36 Liu XZ, Tang CA, Li LC, Lv PF, Liu HY. Microseismic monitoring and 3D finite element analysis of the right bank slope, Dagangshan hydropower station, during reservoir impounding. *Rock Mech Rock Eng.* 2017;50(7):1901–1917.
- 37 Zhou JR, Wei J, Yang TH, Zhu WC, Li LC, Zhang PH. Damage analysis of rock mass coupling joints, water and microseismicity. *Tunn Undergr Space Technol.* 2018;71:366–381.
- 38 Yang JP, Chen WZ, Yang DS, Yuan JQ. Numerical determination of strength and deformability of fractured rock mass by FEM modeling. *Comput Geotech.* 2015;64:20–31.
- 39 Yang TH, Wang PT, Xu T, et al. Anisotropic characteristics of jointed rock mass: a case study at Shirengou iron ore mine in China. *Tunn Undergr Space Technol.* 2015;48:129–139.
- 40 Mazars J, Pijaudiercabot G. Continuum damage theory-application to concrete. *J. Eng. Mech.-ASCE.* 1989;115(2):345–365.
- 41 Tang CA, Tang SB, Gong B, Bai HM. Discontinuous deformation and displacement analysis: from continuous to discontinuous. *Sci China Technol Sci.* 2015;58(9):1567–1574.
- 42 Gui Y, Zhao GF. Modelling of laboratory soil desiccation cracking using DLSM with a two-phase bond model. *Comput Geotech.* 2015;69:578–587.
- 43 Sun PF, Yang TH, Yu QL, Shen W. Numerical research on anisotropic mechanical parameters of fractured rock mass. *Adv Mater Res.* 2012;524–527:310–316.
- 44 Chong ZH, Yao QL, Li XH, Shivakumar K. Acoustic emission investigation on scale effect and anisotropy of jointed rock mass by the discrete element method. *Arabian J Geosci.* 2020;13:324.
- 45 Zhou JX, Zhou Y, Gao YT. Effect mechanism of fractures on the mechanics characteristics of jointed rock mass under compression. *Arabian J Sci Eng.* 2018;43(7):3659–3671.
- 46 Cui Z, Zhang YH, Sheng Q, Cui L. Investigating the scale effect of rock mass in the Yangfanggou hydropower plant with the discrete fracture network engineering approach. *Int J GeoMech.* 2020;20(4), 04020033.
- 47 Zhou Y, Wu SC, Gao YT, Misra A. Macro and meso analysis of jointed rock mass triaxial compression test by using equivalent rock mass (ERM) technique. *J. Cent. South Univ.* 2014;21(3):1125–1135.
- 48 Fan X, Kulatilake P, Chen X. Mechanical behavior of rock-like jointed blocks with multi-non-persistent joints under uniaxial loading: a particle mechanics approach. *Eng Geol.* 2015;190:17–32.
- 49 Liu XB, He SH, Wang DH. Numerical analysis of the anisotropy and scale effects on the strength characteristics of defected rockmass. *Adv Civ Eng.* 2020;2020, 5892924.
- 50 Cui Z, Sheng Q, Leng XL. Study on structural effect of equivalent elastic modulus of columnar jointed rock mass. In: *Proceedings of the 3rd International Conference on Machinery, Materials and Information Technology Applications. Qingdao; 28-29 November.* 2015:1599–1607.
- 51 Pariseau WG, Puri S, Schmelter SC. A new model for effects of impersistent joint sets on rock slope stability. *Int J Rock Mech Min Sci.* 2008;45(2):122–131.
- 52 Vallier F, Mitani Y, Boulon M, Esaki T, Pellet F. A shear model accounting scale effect in rock joints behavior. *Rock Mech Rock Eng.* 2010;43(5):581–595.
- 53 Zheng BW, Qi SW, Huang XL, et al. An advanced shear strength criterion for rock discontinuities considering size and low shear rate. *Appl. Sci.-Basel.* 2020;10(12):4095.
- 54 Lin H, Xie SJ, Yong R, Chen YF, Du SG. An empirical statistical constitutive relationship for rock joint shearing considering scale effect. *Compt Rendus Mec.* 2019;347(8):561–575.
- 55 Wang PT, Ren FH, Cai MF. Influence of joint geometry and roughness on the multiscale shear behaviour of fractured rock mass using particle flow code. *Arabian J Geosci.* 2020;13(4).
- 56 Fardin N, Stephansson O, Jing LR. The scale dependence of rock joint surface roughness. *Int J Rock Mech Min Sci.* 2001;38(5):659–669.
- 57 Niazmandi MM, Binesh SM. A DFN-DEM approach to study the influence of confinement on the REV size of fractured rock masses. *Iran. J. Sci. Technol.-Trans. Civ. Eng.* 2020;44:587–601.
- 58 Stavrou A, Murphy W. Quantifying the effects of scale and heterogeneity on the confined strength of micro-defected rocks. *Int J Rock Mech Min Sci.* 2018;102:131–143.
- 59 Wu Q, Kulatilake P. REV and its properties on fracture system and mechanical properties, and an orthotropic constitutive model for a jointed rock mass in a dam site in China. *Comput Geotech.* 2012;43:124–142.
- 60 Yang T, Liu HY, Tang CA. Scale effect in macroscopic permeability of jointed rock mass using a coupled stress-damage-flow method. *Eng Geol.* 2017;228:121–136.
- 61 Wu N, Liang ZZ, Li YC, Li H, Li WR, Zhang ML. Stress-dependent anisotropy index of strength and deformability of jointed rock mass: insights from a numerical study. *Bull Eng Geol Environ.* 2019;78(8):5905–5917.